# Please cite the Published Version

Zhang, Ting, Peng, Yonghong , Qian, Yu, Zhou, Jianguo and Yin, Xianfei (2025) A Discrete Boltzmann Approach for Numerical Simulation of Wetting and Drying in Shallow Flows. Water Resources Research, 61 (11). e2025WR041568 ISSN 0043-1397

**DOI:** https://doi.org/10.1029/2025WR041568

Publisher: Wiley

Version: Published Version

Downloaded from: https://e-space.mmu.ac.uk/642919/

Usage rights: (cc) BY-NC-ND Creative Commons: Attribution-Noncommercial-No Deriva-

tive Works 4.0

**Additional Information:** This is an open access article published in Water Resources Research, by Wiley.

**Data Access Statement:** The used DBM codes in this paper are available online at https://doi.org/10.5281/zenodo.17211664 (The open-source software program) and were collected by the author (Zhang, 2025).

# **Enquiries:**

If you have questions about this document, contact openresearch@mmu.ac.uk. Please include the URL of the record in e-space. If you believe that your, or a third party's rights have been compromised through this document please see our Take Down policy (available from https://www.mmu.ac.uk/library/using-the-library/policies-and-guidelines)



# Water Resources Research



# **RESEARCH ARTICLE**

10.1029/2025WR041568

#### **Key Points:**

- A discrete Boltzmann model with a wetting-drying treatment is introduced to accurately capture shallow-water flows over complex terrain
- The performance of proposed approach is validated by six classical benchmark tests
- Properly selecting the two threshold water depths is vital for balancing computational stability with accurate simulation results

#### Correspondence to:

Y. Peng, pengyongscu@foxmail.com

#### Citation:

Zhang, T., Peng, Y., Qian, Y., Zhou, J., & Yin, X. (2025). A discrete Boltzmann approach for numerical simulation of wetting and drying in shallow flows. *Water Resources Research*, 61, e2025WR041568. https://doi.org/10.1029/2025WR041568

Received 7 JUL 2025 Accepted 30 OCT 2025

#### **Author Contributions:**

Methodology: Ting Zhang, Yong Peng Resources: Yu Qian Software: Ting Zhang, Xianfei Yin Supervision: Yong Peng, Jianguo Zhou Validation: Ting Zhang Visualization: Yu Qian, Xianfei Yin Writing – original draft: Ting Zhang Writing – review & editing: Jianguo Zhou

#### © 2025. The Author(s).

This is an open access article under the terms of the Creative Commons
Attribution-NonCommercial-NoDerivs
License, which permits use and
distribution in any medium, provided the original work is properly cited, the use is non-commercial and no modifications or adaptations are made.

# A Discrete Boltzmann Approach for Numerical Simulation of Wetting and Drying in Shallow Flows

Ting Zhang<sup>1</sup>, Yong Peng<sup>1</sup>, Yu Qian<sup>2</sup>, Jianguo Zhou<sup>3</sup>, and Xianfei Yin<sup>4</sup>

<sup>1</sup>College of Water Resources and Architectural Engineering, Northwest A&F University, Yangling, China, <sup>2</sup>School of Civil and Environmental Engineering, Ningbo University, Ningbo, China, <sup>3</sup>Department of Computing and Mathematics, Manchester Metropolitan University, Manchester, UK, <sup>4</sup>Department of Architecture and Civil Engineering, City University of Hong Kong, Hong Kong, China

**Abstract** Wetting and drying processes in shallow-water flows remain challenging to simulate accurately, especially over complex terrain where conventional methods often struggle to maintain stability and precision. To address this gap, a discrete Boltzmann model is developed in this study, incorporating an effective wetting and drying treatment to precisely capture the dynamics of wet–dry boundaries across intricate terrain. The model's performance is evaluated through six benchmark tests, including three one-dimensional (1D) and three two-dimensional (2D) cases: (a) flow in a straight channel with a triangular bed obstacle; (b) propagation of one-dimensional tidal waves across a varying sloped bed; (c) dam-break flow over non-uniform terrain with two elevation steps; (d) 2D dam-break in an L-shaped channel; (e) 2D dam-break flow through a contracting channel; and (f) 2D flooding over terrain with three mounds. The numerical results align well with analytical solutions, previously published computational results, and experimental data. Furthermore, the study highlights the critical role of the wetting threshold water depth in determining both accuracy and numerical stability. An excessively high threshold could result in imprecise predictions of wet–dry transitions, while a threshold set too low may cause numerical instability. Therefore, the appropriate selection of this parameter is essential for obtaining reliable and consistent simulations.

# 1. Introduction

Shallow water flows, characterized by horizontal motion, are common hydrodynamic phenomena in nature and play a crucial role in various hydraulic and environmental engineering applications. By assuming hydrostatic pressure and disregarding vertical acceleration, the incompressible Navier–Stokes equations are vertically integrated to derive the nonlinear shallow water equations (SWEs). Over time, numerous numerical approaches have been devised to find approximate solutions to the nonlinear SWEs, including the finite difference method (Bulatov & Elizarova, 2011; Jiang et al., 2023; Magdalena & Pebriansyah, 2022), the finite volume method (Kesserwani & Wang, 2014; Liu, 2020; Zhou et al., 2004), and the finite element method (Aizinger & Dawson, 2002; Liang et al., 2020). These approaches work efficiently on uniform grids and under regular boundary conditions. However, they face limitations related to mass conservation, numerical stability, and scalability when applied to complex topography, obstacle interference, and dynamic wetting-drying interfaces.

The lattice Boltzmann method (LBM) is known as a mesoscopic numerical technique grouped in statistical physics (Dellar, 2002; Mcnamara & Zanetti, 1998; Qian et al., 1992), which has become a focal point in computational fluid dynamics (Kefayati et al., 2023; Li et al., 2015; Liu et al., 2021; Liu & Zhou, 2010; Perumal & Dass, 2015; Rocca et al., 2012; Stipić et al., 2022; Zhou, 2002). The advantages of LBM include its algorithmic simplicity, ease in dealing with complex boundary treatments, and high parallelization efficiency. These features make it particularly well-suited for simulating free-surface flows and geometrically intricate domains. Consequently, LBM has found widespread application in shallow water flow modeling (Thömmes et al., 2007; Venturi, 2018). Peng et al. (2014) conducted simulations of shallow water flows over discontinuous riverbeds using LBM. Thorimbert et al. (2019) combined a two-dimensional free-surface LBM with a one-dimensional shallow water LBM to reduce computational costs. More recently, Ru et al. (2024) proposed a new LBM framework for multilayer SWEs.

A persistent challenge in shallow water flow simulations is the accurate representation of supercritical flow phenomena (Hedjripour, 2018; Hedjripour et al., 2016). To overcome this limitation, La Rocca et al. (2015) introduced a specific multi-speed discrete Boltzmann equation and successfully modeled supercritical flows.

ZHANG ET AL. 1 of 25

Subsequently, Meng et al. (2018) discretized the particle velocity space of the continuous Boltzmann equation using Hermite expansion and Gauss-Hermite quadrature, resulting in discrete velocity models. These models can lead to both single-speed DBM and various high-order DBMs for various flow regimes. For numerical implementation, spatial discretization is achieved using the finite difference method, whereas temporal discretization is performed with a forward Euler scheme, ensuring that the conservation laws are automatically satisfied.

Wetting and drying processes along coastlines and riverbanks are common and critical phenomena in shallow water flows. Proper handling of these processes is essential, as it significantly affects the stability and accuracy of numerical simulations (Castro et al., 2005; Kalita & Sarma, 2018; Sobey, 2009; Vater et al., 2015; Xia et al., 2010). Generally, two principal strategies are usually employed to model wetting and drying: Lagrangian and Eulerian approaches (Funke et al., 2011; Quecedo & Pastor, 2002). The Lagrangian approach offers high accuracy by explicitly tracking the moving interface, but it often requires complex mesh adaptation techniques, making it difficult to implement in practical engineering problems, especially under complex topographic conditions. In contrast, the Eulerian approach is more straightforward to implement and computationally efficient. However, a key challenge lies in achieving accurate interface tracking while maintaining numerical stability (Hou et al., 2013; Song et al., 2011). Among Eulerian strategies, the thin film approach (Oey, 2005) and the minimum threshold approach (Cozzolino et al., 2012; Le et al., 2020) are widely used due to their reliable robustness and broad applicability (Liu & Zhou, 2014; Xia et al., 2010; Zhang et al., 2025). Early implementations of minimum threshold theory, similar wetting-drying treatments were proposed by Zhao et al. (1994) and Sleigh et al. (1998). He & Xin. (2009) provided further insights into the treatment of wet-dry boundaries in the context of SWEs. Shafiai (2011) combined the thin film method with a linear interpolation scheme to investigate wetting and drying processes. Liu et al. (2016, 2017) developed a wetting-drying scheme with second-order accuracy for shallow water flows, formulated within the lattice Boltzmann framework and derived using Chapman-Enskog and Taylor series expansions. Despite these advances, research on wetting and drying treatments within multi-speed DBMs remains relatively limited, highlighting a need for further research in this area.

In this study, the multi-speed DBM incorporates the wetting and drying strategy developed by Zhao et al. (1994) and Sleigh et al. (1998) to simulate and evaluate shallow water flow dynamics involving wet–dry transitions. To thoroughly evaluate the effectiveness of the proposed strategy, six classical benchmark test cases are employed. The subsequent content of this paper is arranged as outlined below: Section 2 outlines the DBM formulation for shallow water flow modeling; Section 3 details the implementation of the wetting-drying strategy; Section 4 describes the boundary conditions; Section 5 presents the model evaluation; Section 6 provides validation and application results; Section 7 delivers the synthesis and discussion.

#### 2. Discrete Boltzmann Shallow Water Model

The depth-averaged governing equations for two-dimensional shallow water flow are given by (Zhou, 2002),

$$\frac{\partial h}{\partial t} + \nabla \cdot (h\mathbf{u}) = 0,\tag{1}$$

$$\frac{\partial(hu)}{\partial t} + \nabla \cdot (huu) = -\nabla P + \nu \nabla \cdot \nabla (hu) + F, \tag{2}$$

where, h denotes the water depth, g is the gravitational acceleration (9.81 m/s<sup>2</sup>), u represents the depth-averaged flow velocity,  $\nu$  is the depth-averaged molecular kinematic viscosity coefficient, and t represents time. The source term  $F = (F_x, F_y)$  is defined as:

$$F = -gh\frac{\partial z_b}{\partial x} - \frac{\tau_b}{\rho}.$$
 (3)

The bed shear stress  $\tau_b$  is expressed as follows:

$$\tau_h = \rho C_h u \sqrt{u \cdot u}. \tag{4}$$

The bed friction coefficient  $C_b$  is a dimensionless parameter that can be computed as follows:

ZHANG ET AL. 2 of 25

$$C_b = \frac{g}{C_z^2},\tag{5}$$

in which,  $C_z = \frac{h^{\frac{1}{6}}}{n_b}$  denotes Chezy's coefficient, while  $n_b$  represents Manning's roughness coefficient.

To facilitate the analysis of the DBM, the physical quantities are first nondimensionalized, yielding the dimensionless form of the governing equations:

$$\hat{h} = \frac{h}{h_0}, \hat{V} = \frac{\sqrt{2}V}{\sqrt{gh_0}}, \hat{r} = \frac{r}{h_0}, \hat{P} = \frac{P}{P_0} = \hat{h}^2$$
 (6)

$$\hat{c} = \frac{\sqrt{2}c}{\sqrt{gh_0}}, \hat{t} = \frac{\sqrt{gh_0}}{\sqrt{2}h_0}, \hat{v} = \frac{v}{v_0}, \hat{F} = \frac{2F}{g}, \tag{7}$$

In the above equation, variables with hats (e.g.,  $\hat{h}$ ,  $\hat{V}$ ) denote their dimensionless form. The reference length  $h_0$  serves as the characteristic scale used in the numerical simulation.

In the DBM, a discrete kinetic equation is employed instead of directly resolving the SWEs,

$$\frac{\partial f_{\alpha}}{\partial t} + c_{\alpha} \cdot \frac{\partial f_{\alpha}}{\partial \mathbf{x}} = -\frac{1}{\tau} (f_{\alpha} - f_{\alpha}^{eq}) + \mathbf{F}_{\alpha}. \tag{8}$$

Describing the evolution at a specific time t and location x, the fundamental variable is the discrete distribution function  $f_{\alpha}(x,t)$ , which is tied to particular velocity directions  $c_{\alpha}$ . Macroscopic quantities including water depth and flow velocity are obtained by performing moment operations on these distribution functions,

$$h = \sum_{\alpha} f_{\alpha} = \sum_{\alpha} f_{\alpha}^{eq},\tag{9}$$

$$\boldsymbol{u} = \frac{1}{h} \sum_{\alpha} f_{\alpha} \boldsymbol{c}_{\alpha} = \frac{1}{h} \sum_{\alpha} f_{\alpha}^{eq} \boldsymbol{c}_{\alpha},\tag{10}$$

The body force is represented at the mesoscopic level by the following additional source term,

$$\mathcal{F}_{a} = h\omega_{a} \left[ F(\mathbf{x}, t) \cdot \mathbf{c}_{a} \right], \tag{11}$$

The symbol  $\tau = \kappa/\hat{h}$  denotes the dimensionless relaxation time. It is worth emphasizing that  $\kappa$  can be expresses as  $\kappa = \frac{\nu_0 \sqrt{gh_0/2}}{\phi h^2/2}$ .

To model supercritical flow, the equilibrium distribution function is employed in the following fourth-order form (Meng et al., 2018; Peng et al., 2024),

$$f_{\alpha}^{eq} = h\omega_{\alpha} \begin{pmatrix} 1 + c_{\alpha} \cdot \boldsymbol{u} + \frac{1}{2} ((c_{\alpha} \cdot \boldsymbol{u})^{2} - \boldsymbol{u} \cdot \boldsymbol{u} + (h - 1) (c_{\alpha} \cdot c_{\alpha} - 2)) \\ + \frac{c_{\alpha} \cdot \boldsymbol{u}}{6} ((c_{\alpha} \cdot \boldsymbol{u})^{2} - 3\boldsymbol{u} \cdot \boldsymbol{u} + 3(h - 1) (c_{\alpha} \cdot c_{\alpha} - 4)) \\ + \frac{1}{24} ((c_{\alpha} \cdot \boldsymbol{u})^{4} - 6(c_{\alpha} \cdot \boldsymbol{u})^{2} \boldsymbol{u} \cdot \boldsymbol{u} + 3(\boldsymbol{u} \cdot \boldsymbol{u})^{2}) \\ + \frac{h - 1}{4} ((c_{\alpha} \cdot c_{\alpha} - 4) ((c_{\alpha} \cdot \boldsymbol{u})^{2} - \boldsymbol{u} \cdot \boldsymbol{u}) - 2(c_{\alpha} \cdot \boldsymbol{u})^{2}) \\ + \frac{(h - 1)^{2}}{8} ((c_{\alpha} \cdot c_{\alpha})^{2} - 8c_{\alpha} \cdot c_{\alpha} + 8) \end{pmatrix}$$
(12)

ZHANG ET AL. 3 of 25

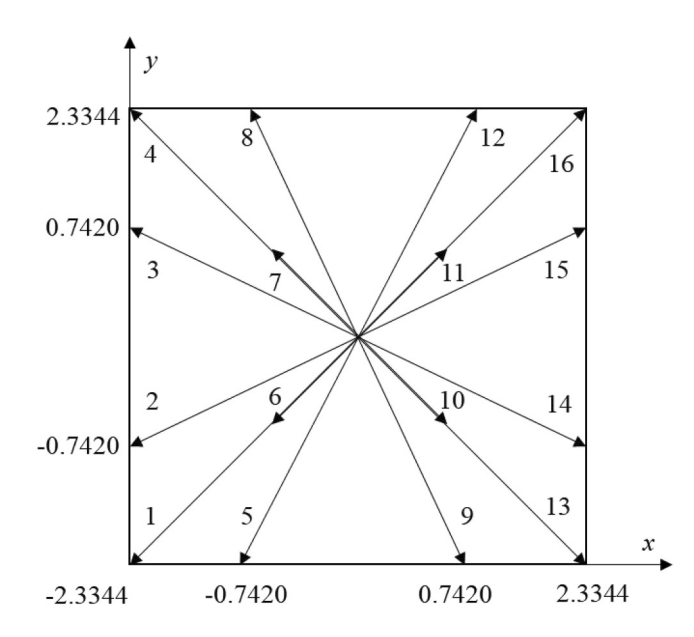


Figure 1. Schematic of the D2Q16 lattice pattern.

Figure 1 shows the D2Q16 model adopted in the DBM.

The coordinate values shown in Figure 1 correspond to the discrete velocities, whose weights are given by the following expressions:

$$\omega_{\alpha} = \begin{cases} 0.002104594 & \alpha = 1, 4, 13, 16 \\ 0.020833333 & \alpha = 2, 3, 5, 8, 9, 12, 14, 15 \\ 0.206228739 & \alpha = 6, 7, 10, 11 \end{cases}$$
 (13)

In high-order expansions, the discrete velocities become non-integer values, making the collision-transport scheme inapplicable to Equation 8. To tackle this problem, this study adopts a straightforward finite-difference approach for both temporal and spatial discretization. Specifically, an upwind scheme is utilized for spatial discretization to effectively capture flow features and ensure numerical stability, while a forward Euler method is employed for temporal discretization, offering simplicity and computational efficiency. This combination provides a practical and robust numerical strategy to address the limitations introduced by non-integer discrete velocities, facilitating accurate simulations of the underlying physical phenomena.

# 3. Treatment of Wetting and Drying in Elements

This study utilizes the wetting and drying approach originally proposed by Zhao et al. (1994) and Sleigh et al. (1998). Two threshold water depths,  $h_{\rm dry}$  and  $h_{\rm wet}$ , are predefined to classify the computational domain into dry, wet, and partially wet cells. The approach used in this model to treat the wet–dry interface is described as follows:

- 1. Dry Cells: The simulation involves monitoring the water depth across all cells in the domain. A cell is considered dry when its water depth falls below the specified dry threshold  $h_{dry}$ , and all its neighboring cells also have water depths below  $h_{dry}$ .
- 2. Wet Cells: A cell is considered wet if its water depth surpasses the threshold value  $h_{\text{wet}}$ . In this case, both momentum and mass fluxes are included in the calculations.
- 3. Partially Wet Cells: Cells with water depth between  $h_{dry}$  and  $h_{wet}$ , or those with the water depth below  $h_{dry}$  but with at least one neighboring cell above  $h_{dry}$ , are classified as a partially wet cell. For these cells, zero is assigned to the momentum flux, while the mass flux is still computed.

In both dry and partially wet cells, we enforce the velocity to be zero. However, the water depth in all cells remains unchanged. Once water depth and velocity are available, the equilibrium distribution function  $f_{\alpha}^{eq}$  is employed to determine the mesoscopic distribution functions in directions that are not yet known at the wet–dry interface.

# 4. Boundary Conditions

Two boundary condition types are adopted in the current model: transmissive and reflective boundary conditions. In numerical simulations, open flow boundaries are typically treated using the transmissive boundary condition, where the macroscopic water depth  $h_m$  and velocity  $u_m = (u_{mn}, v_{mT})$  are prescribed using target values  $h_i$  and  $u_i = (u_{in}, v_{iT})$ , where the subscripts n and T represent the components in the outward normal and tangential directions, respectively. For wall boundary conditions, reflective boundary are commonly implemented, the depth  $h_m$  and the tangential component of velocity  $v_{mT}$  are respectively assigned as  $h_i$  and  $v_{iT}$ , respectively, whereas we set the normal component of velocity  $u_{mn}$  to zero.

After the macroscopic boundary values are specified, the corresponding distribution functions are reconstructed using the non-equilibrium extrapolation method developed by Guo et al. (2002). In this approach, the equilibrium component is computed from the prescribed macroscopic variables, while extrapolation is used to approximate the non-equilibrium component.

ZHANG ET AL. 4 of 25

19447973, 2025, 11, Downloaded from https://agupubs

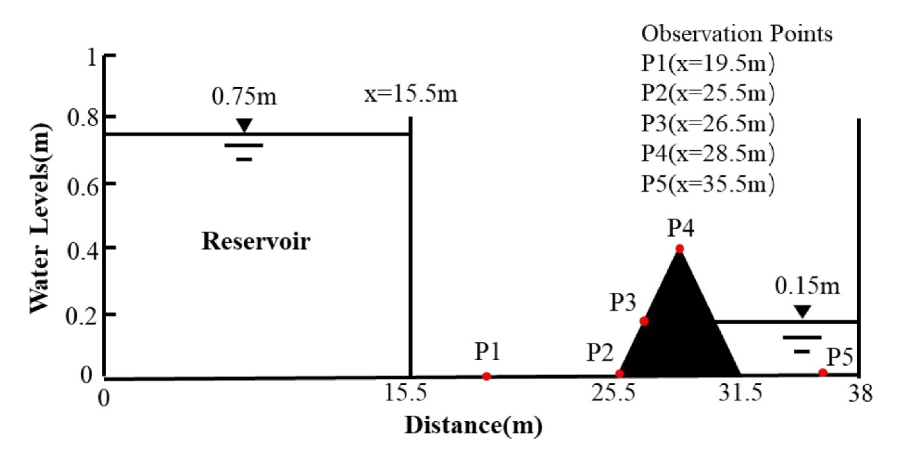


Figure 2. Dam-break flow over a triangular obstacle.

#### 5. Model Evaluation

To assess discrepancies between the model's predicted outcomes and experimental, as well as to assess grid convergence, the relative error is employed, defined as follows:

$$E_r = \frac{1}{N} \sqrt{\sum_{1}^{N} \left[ (h_{\text{nu}} - h_{\text{ex}}) / h_{\text{ex}} \right]^2}$$
 (14)

where  $h_{\text{nu}}$  denotes the water depth predicted by the DBM model,  $h_{\text{ex}}$  represents the experimental measurements, and N is the total number of the lattice points.

# 6. Numerical Simulations and Validation

In this study, we conduct numerical tests to evaluate the effectiveness of the 16-speed DBM in simulating wetting and drying interfaces. Initially, Sections 6.1–6.3 focus on one-dimensional validation cases, including scenarios with bed slope and friction effects, to examine the proposed wetting-drying scheme. The evaluation is then extended in Sections 6.4–6.6 to two-dimensional cases, providing a more comprehensive assessment of the scheme's performance.

# 6.1. Flow Over a Triangular Bed Obstacle in a Straight Channel

This validation case numerically simulates a dam-break experiment conducted at the Université Libre de Bruxelles in Belgium (Waterways Experiment Station, 1960, 1961). The objective is to investigate the influence of complex topography and bed friction on the performance of wetting and drying treatments. The physical model used in the experiment is 38 m long and 1.75 m wide. Initially, a 15.5 m stretch upstream represents a reservoir, where water remains still at a 0.75 m depth, while the remaining bed is a dry and rough. The dam is positioned at x = 15.5 m, and a 0.4 m in height symmetric triangular obstacle is placed downstream between 25.5 and 31.5 m. The channel terminates at a fixed gate, with a still water depth of 0.15 m between the gate and the downstream side of the obstacle (Figure 2). Throughout the experiment, the flow remains within the model boundaries. The bed is assigned a Manning roughness coefficient of 0.0125. The roughness value was chosen according to prior modeling studies on this experiment conducted by Brufau et al. (2002) and Liao et al. (2007). Upon initiating the simulation, the dam is postulated to collapse abruptly in the model, allowing the reservoir water to rush downstream freely. The resulting flow is highly complex due to the influence of slope, bed friction, and wet-dry transitions. To better understand these dynamics, several experimental and numerical studies have been conducted by Hiver (2000), Rebollo et al. (2003), Zhou et al. (2004), and Xia et al. (2010). During the experimental process, In Hiver's experiment water depth variations were recorded at five locations: 19.5, 25.5, 26.5, 28.5, and 35.5 m from the upstream boundary. These measurements provide a basis for comparison with our simulation results.

ZHANG ET AL. 5 of 25

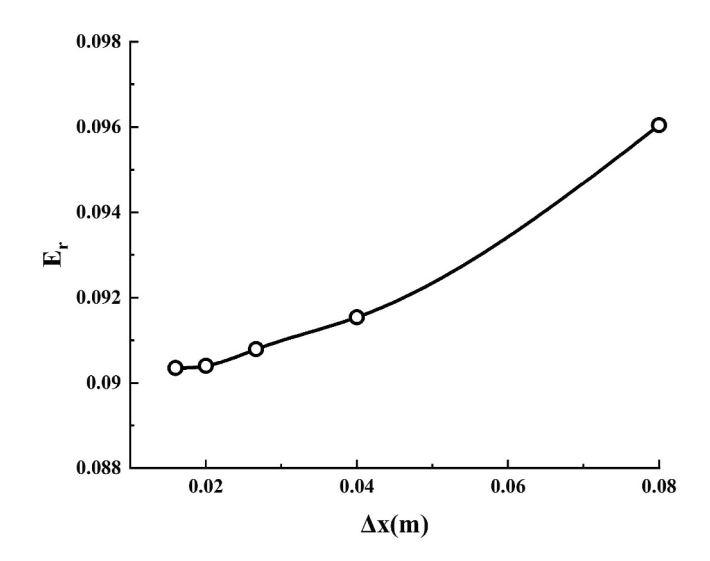


**Figure 3.** Variation of relative error  $E_r$  with grid size  $\Delta x$ .

In this study, a two-dimensional model is utilized to simulate the following one-dimensional cases, and along the secondary spatial dimension (e.g., y-axis), periodic boundary conditions are implemented, requiring two extra computational cell layers for proper numerical treatment. When implementing the wetting-drying boundary treatment, the numerical results exhibit high sensitivity to the selection of two characteristic water depth values. However, it should be noted that these two parameters do not have direct physical significance.

It should also be emphasized that the aforementioned physical parameters can be easily transformed into the non-dimensional form outlined in Section 2. For instance, choosing a reference water depth  $h_0=1$  m yields a corresponding reference velocity of  $\sqrt{gh_0/2}\approx 2.215$ . The same method can be applied to nondimensionalize other relevant quantities. Other variables can be dimensionless in a similar fashion. Although the following simulations may adopt the non-dimensional framework internally, all results are uniformly expressed in physical units for clarity and ease of interpretation.

A grid convergence study was conducted by discretizing the *x*-direction into meshes that increased in multiples of 475 cells, ranging from 475 up to 2,375.

The relative error, calculated at t=15s based on the water depth discrepancies at five gauge locations compared with the experimental measurements, was employed as the evaluation criterion. Figure 3 demonstrates a clear reduction in error as the mesh is refined from coarse to intermediate resolutions, with noticeable improvement up to a mesh resolution of 0.02666 m. Beyond this point, further refinement to 0.02 and 0.016 m produces only marginal changes, indicating that the solution has essentially reached grid convergence. Consequently, the 1900-cell mesh was selected for subsequent simulations as it achieves a balance between numerical accuracy and computational efficiency.

A uniform grid of  $1900 \times 2$  cells is used to discretize the domain in the length and width directions, using a time step of 0.0001s. Since  $h_{\rm dry}$  and  $h_{\rm wet}$  are critical parameters affecting the simulations, five sets of values were tested in this case: Case A ( $h_{\rm dry} = 0.00075$  m,  $h_{\rm wet} = 0.0075$  m), Case B ( $h_{\rm dry} = 0.00375$  m,  $h_{\rm wet} = 0.0075$  m), Case C ( $h_{\rm dry} = 0.00375$  m,  $h_{\rm wet} = 0.0075$  m), Case D ( $h_{\rm dry} = 0.0075$  m), and Case E ( $h_{\rm dry} = 0.00075$  m,  $h_{\rm wet} = 0.00075$  m), in order to investigate their influence on the numerical accuracy and stability. Correspondingly, the reference length  $h_0$  is taken as 1 m and  $\tau = 0.0001$ .

As shown in Figure 4, comparative results between simulated and observed water depths at five monitoring points are presented. At point P1, a slight rise in water level occurs around 27s after the dam break, resulting from the downstream flood wave reflecting off the outlet side wall and propagating upstream. After passing over the obstacle, the reflected wave reaches P1, causing a localized increase in water level. A similar rise occurs at point P2 around 24s, due to the same mechanism. However, in the simulation, this response appears approximately 2s earlier than in the experiment. Additionally, the predicted water depth at P2, computed using the discrete Boltzmann shallow water model, is generally higher than the observed experimental value. This discrepancy has also been noted in previous studies (Rebollo et al., 2003). There are two main reasons for this deviation: (a) the enclosed computational domain leads to energy dissipation within the system, intensifying turbulence near this location; (b) P2 is positioned at the upstream corner of the obstacle, where the boundary layer separation and vortex formation occur, violating the hydrostatic pressure assumption of the SWEs. At P3, the numerical simulation results closely match the experimental measurements. However, due to the discontinuity in experimental sampling time, the observed data failed to capture the water surface rise caused by upstream reflected waves, which does not reflect the actual behavior. Point P4 is placed at the peak of the obstacle, shoes slightly lower simulated water depths than the experimental observations, which likely results from the neglect of vertical acceleration in the SWEs and the local topographical discontinuity of the obstacle. Nevertheless, these results align well with those documented in previous studies. At P5, which lies downstream of the obstacle, the numerical model accurately captures the fluctuations of the passing wave crests and troughs, demonstrating good agreement with the experimental observations.

ZHANG ET AL. 6 of 25

19447973, 2025, 11, Downloaded from https://agupubs

onlinelibrary.wiley.com/doi/10.1029/2025WR041568 by Manchester Metropolitan University, Wiley Online Library on [14/11/2025]. See the Terms and Conditions (https://onlinelibrary.wiley.

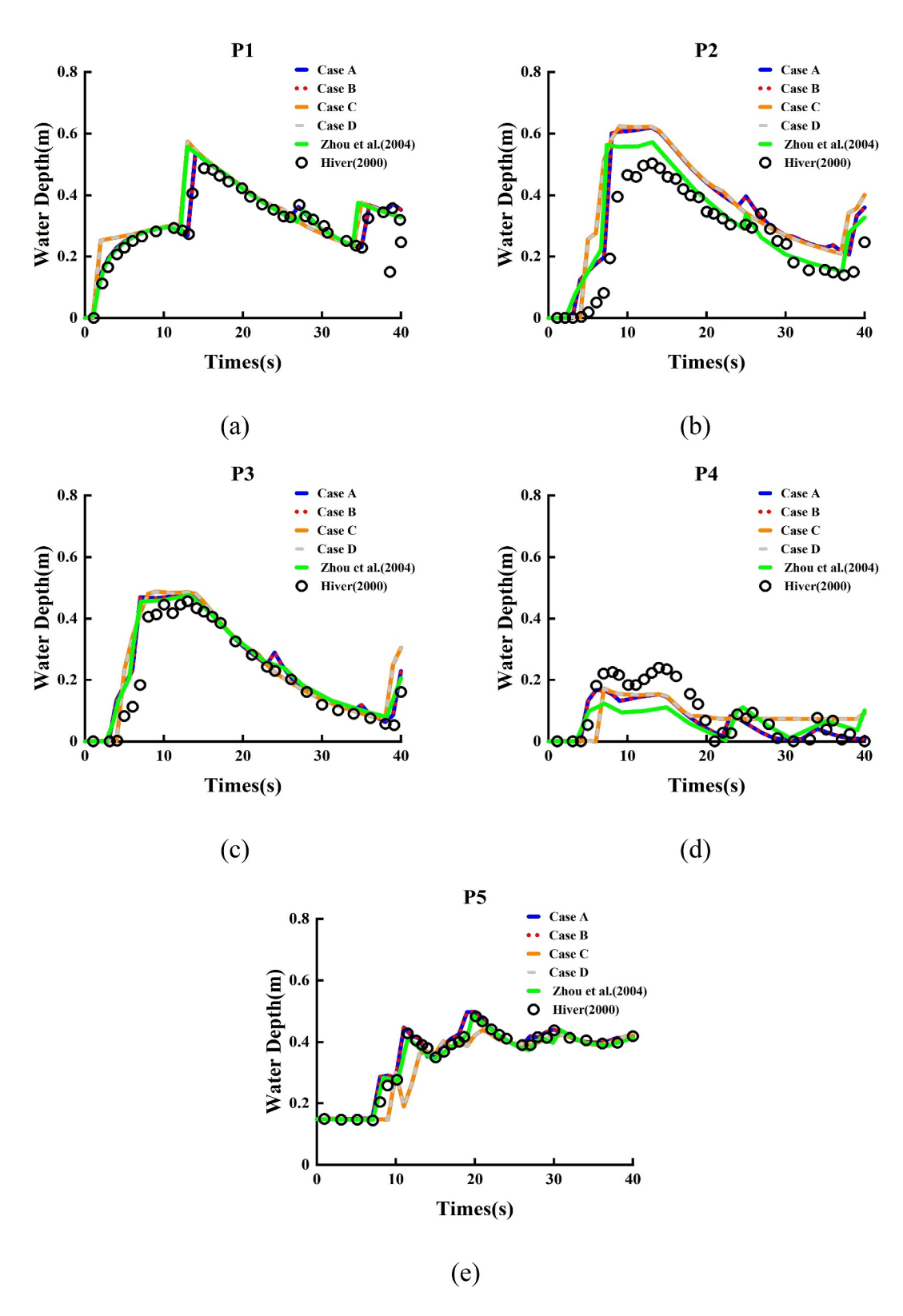


Figure 4. Comparisons of water depth between model predictions and measurements at different locations.

ZHANG ET AL. 7 of 25

19447973, 2025, 11, Downle

Case	$h_{\rm dry}$ (m)	h <sub>wet</sub> (m)	Average relative errors	Stability remark
A	0.00075	0.0075	0.12954	Stable
В	0.00375	0.0075	0.13023	Stable
C	0.00375	0.075	0.33151	Stable
D	0.0075	0.075	0.33376	Stable
E	0.000075	0.00075	-	Unstable

In addition to these local discrepancies, further simulations with varying wet—dry thresholds revealed that the choice of  $h_{\rm dry}$  and  $h_{\rm wet}$  has a non-negligible influence on accuracy and stability, with the impact of  $h_{\rm wet}$  being particularly pronounced. Figure 4 also compares the simulated and experimental water depths for selected threshold values. Stable simulations are obtained for moderate and large thresholds, with Case C and D effectively suppressing instability but producing results with significant errors compared to experimental measurements. In contrast, Case A achieves the optimal balance, yielding stable simulations with good agreement with the experimental data. Whereas very small thresholds (e.g., Case E) led to divergence and are therefore not shown in the figure. Table 1 summarizes the corresponding error metrics

# 6.2. Propagation of One-Dimensional Tidal Waves Across a Varying Sloped Bed

The present case investigates tidal wave propagation over a riverbed with a non-uniform slope. Leclerc et al. (1990) and Liu and Zhou. (2014) have conducted simulations of this case. The channel spans 500 m in total, and the longitudinal bed slope ( $S = dz_b/dx$ ) of the channel is provided in Table 2. The initial water level throughout the channel is set at 1.75 m. At x = 0 m, a solid wall boundary is implemented, while an inflow boundary condition is specified at x = 500 m, which is influenced by the post-tidal water depth variation (see Figure 5) and can be defined by the following expression:

$$h(500,t) = A + \lambda \cos\left(2\pi \frac{t}{T}\right),\tag{15}$$

Here, the reference water surface is set as A = 1 m, the tidal period is T = 3600s, and the amplitude of the tidal wave is  $\lambda = 0.75$  m.

In addition, for the riverbed, the value of the Manning roughness coefficient is set to 0.03. A uniform grid of  $500 \times 2$  cells is used to discretize the computational domain, with a time step of dt = 0.02s. The characteristic dry water depth  $h_{\rm dry}$  is set to 0.0001 m, and the characteristic wet water depth  $h_{\rm wet}$  is set to 0.001 m. The reference water depth  $h_0$  is taken as 1 m, and the relaxation time  $\tau$  is set to 0.1.

As shown in Figure 6, the simulated tidal run-up water surface and velocity profiles at t=3240s show excellent consistency with the numerical results reported by Leclerc et al. (1990) and Heniche et al. (2000), whose reference data are also shown in the figure. Similarly, Figure 7 demonstrates consistent variations in the flow velocity and water surface to the results of the two aforementioned studies, successfully reproducing the tidal wave propagation along the coast. These simulation results validate the model's reliability in representing the wetting–drying interface across both temporal and spatial dynamics.

#### 6.3. Dam-Break Flow Over Non-Uniform Terrain With Two Elevation Steps

In this study, Aureli et al.'s (1999) dam-break experiment serves as a reference case to validate the effectiveness of the wetting-drying approach. This benchmark incorporates a wide range of complex phenomena that pose significant challenges for numerical models in realistic flood simulations. These include wave reflections, dynamic wetting and drying, irregular topography, high roughness condition, and the requirement to maintain steady-state solutions.

The simulation domain is defined by a 7 m channel featuring two raised trapezoidal humps, designated as A and B. The dam is initially positioned at the crest of Hump A, while Hump B is located near the downstream outlet. A

 Table 2

 Bed Slopes
 x(m)
 0-100
 100-200
 200-500

 S
 -0.001
 -0.01
 -0.001

reservoir located upstream of the dam contains still water at an initial depth of 0.45 m, with the remainder of the channel initially dry. A solid wall condition is applied at the upstream boundary, whereas a free outflow is specified downstream boundary. Figure 8 presents the setup diagram, and the bed roughness is characterized by a Manning coefficient of 0.01. The domain is discretized into  $350 \times 2$  grid cells. A reference length of  $h_0 = 1$  m is used, with threshold depths for dry and wet states defined as  $h_{\rm dry} = 0.0001$  m and

ZHANG ET AL. 8 of 25

19447973, 2025, 11, Downle

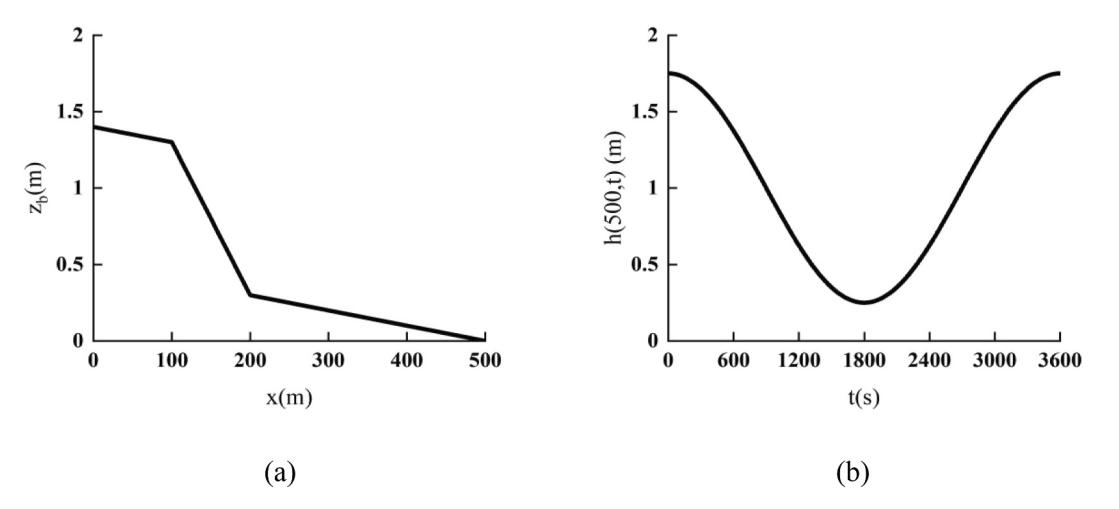


Figure 5. (a) Riverbed elevation profile and (b) inlet boundary condition.

 $h_{\rm wet} = 0.001$  m, respectively. The time step is fixed at 0.0001s, and the relaxation time  $\tau$  is set to 0.0001.

The time—dependent changes in water depth at x = 1.4 m, 2.25 m, and 4.5 m are depicted in Figure 9. A comparison is made between the numerical predictions, experimental measurements, and the simulations conducted by Aureli et al. (1999). The simulated water depths at the three measurement locations exhibit excellent agreement with the experimental observations and are generally consistent with numerical results from Aureli et al. (1999). The model demonstrates strong capability in predicting the wetting and drying dynamics in the downstream region. However, both simulations reveal a minor delay in flood wave arrival, which is likely attributable to the omission of vertical acceleration effects in the SWEs. Figure 10 presents the time-varying curves of Froude numbers at three measuring points, among which the Froude number at the point corresponding to Figure 10c changes extremely drastically, reflecting the intense degree of flow pattern variation at this location.

#### 6.4. 2D Dam-Break in an L-Shaped Channel

In the present test case, Frazao and Zech. (2002) performed experiments on dam-break flows. The setup consisted of a rectangular reservoir connected to a downstream channel arranged in an L-shaped layout. This configuration has since been widely adopted in numerical studies by several researchers (Gottardi & Venutelli, 2004; Liu et al., 2013; Wood & Wang, 2015; Zhang & Wu, 2011). Figure 11 presents a top-view illustration of the

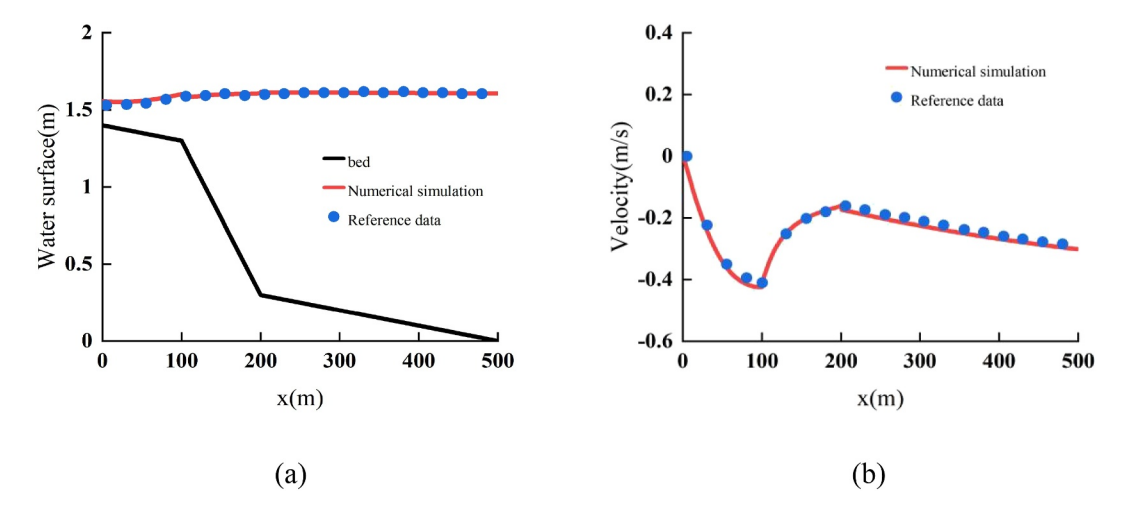


**Figure 6.** Simulated water surface and velocity profiles at t = 3240s.

ZHANG ET AL. 9 of 25

19447973, 2025, 1,1 Downloaded from https://agupubs.onlinelibrary.wiley.com/doi/10.1029/2025WR041568 by Manchester Metropolitan University. Wiley Online Library on [14/11/2025]. See the Terms and Conditions (https://onlinelibrary.wiley.com/erms

and-conditions) on Wiley Online Library for rules of use; OA articles are governed by the applicable Creat

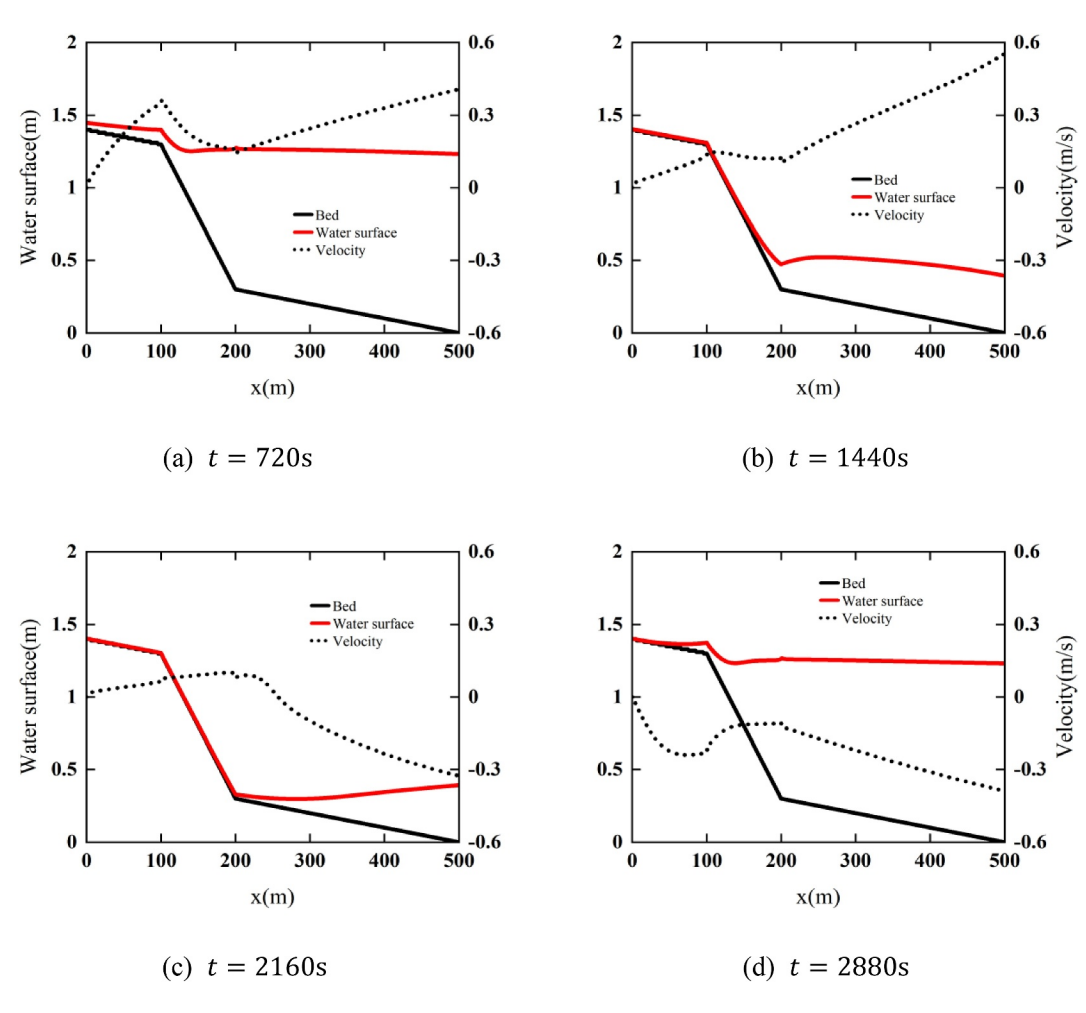


Figure 7. Temporal variation of velocity and water level in a basin with a non-uniform slope.

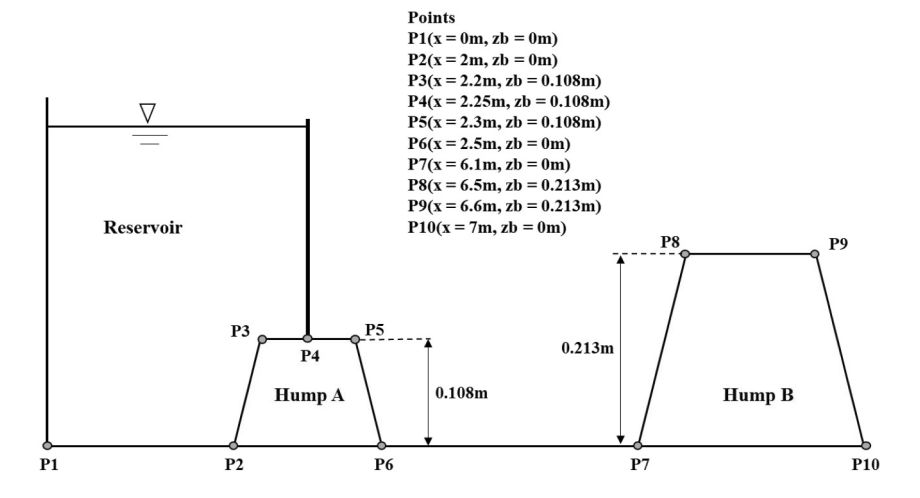


Figure 8. Layout of the physical model for dam-break flow over two elevation steps.

ZHANG ET AL. 10 of 25

19447973, 2025, 11, Downloaded from https://agupubs

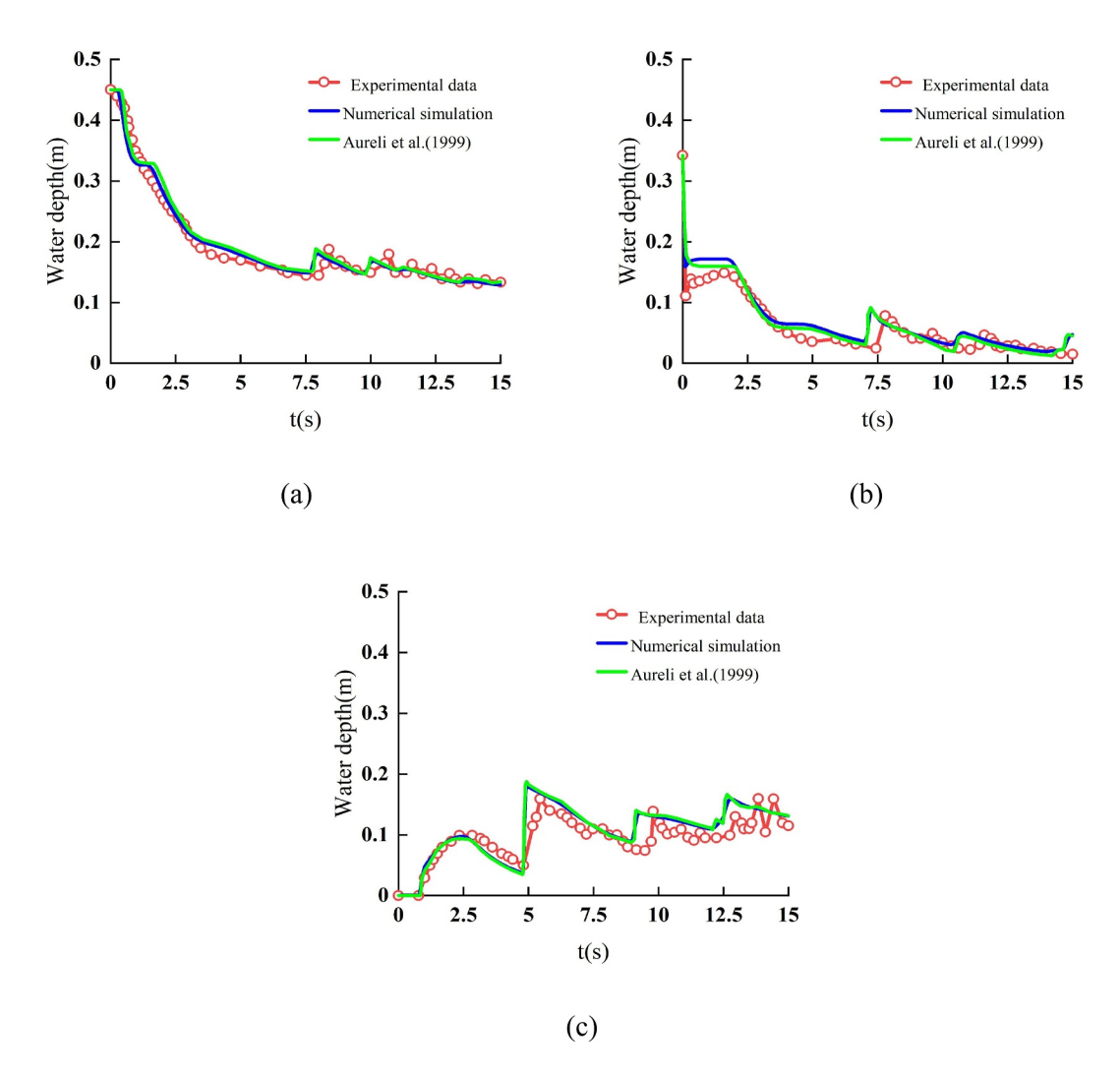


Figure 9. Comparison of predicted and experimental time histories of water depth at (a) x = 1.4 m, (b) 2.25 m, and (c) 4.5 m.

experimental arrangement, including the locations of six measurement points (G1 (1.19 m, 1.2 m), G2 (2.74 m, 0.6925 m), G3 (4.24 m, 0.6925 m), G4 (5.74 m, 0.6925 m), G5 (6.5575 m, 1.51 m), G6 (6.5575 m, 3.01 m)). The reservoir is a rectangular tank measuring  $2.39 \text{ m} \times 2.44 \text{ m}$  and is connected to a  $90^{\circ}$  L-shaped channel. The initial condition features a reservoir with a water depth of 0.2 m. The flow resulting from the dam break begins when the gate, which originally divides the reservoir and the channel, is abruptly removed. Downstream conditions accounted for both wet and dry bed cases, with the wet-bed case assuming a channel water depth of 0.01 m, while in the dry-bed condition, no initial water present. A Manning coefficient of 0.012 is applied to the flat channel bed. Reflective conditions are applied to the upstream boundary and side walls, whereas the downstream boundary allows free outflow.

In the present simulation, a uniform 1361  $\times$  772 cell grid is used, with a time step of 0.0005s. To ensure numerical stability and accuracy, the dry threshold depth  $h_{\text{dry}}$  is set to 0.001 m, and the wet threshold depth  $h_{\text{wet}}$  is set to 0.02 m. A reference length of  $h_0 = 0.2$  m and a relaxation parameter  $\tau = 0.004$  are adopted. It is assumed that the gate opens instantaneously at t = 0s, and the simulation is carried out until t = 40s.

Figure 12 compares the computed water depth with the experimental measurements under dry-bed downstream condition, showing a high level of agreement. Similar simulation results have also been observed in the study by Liu et al. (2013). At (a) G1, the free surface elevation in the reservoir shows a rapid decrease within the first 15s

ZHANG ET AL. 11 of 25

19447973, 2025, 11, Downloaded from https://agupubs.onlinelibrary.wiley.com/doi/10.1029/2025WR041568 by Manchester Metropolitan University, Wiley Online Library on [14/11/2025]. See the Terms

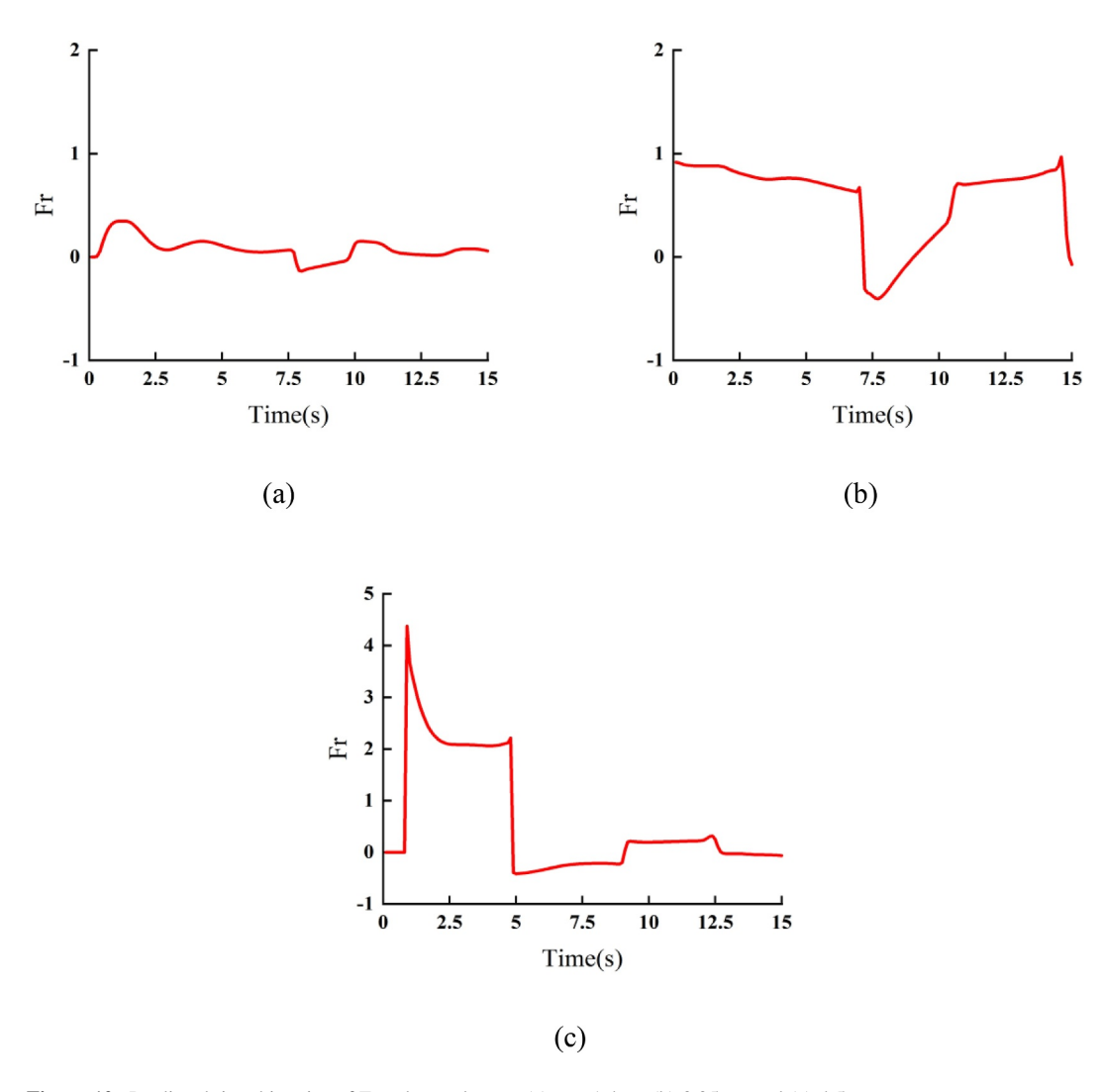


Figure 10. Predicted time histories of Froude numbers at (a) x = 1.4 m, (b) 2.25 m, and (c) 4.5 m.

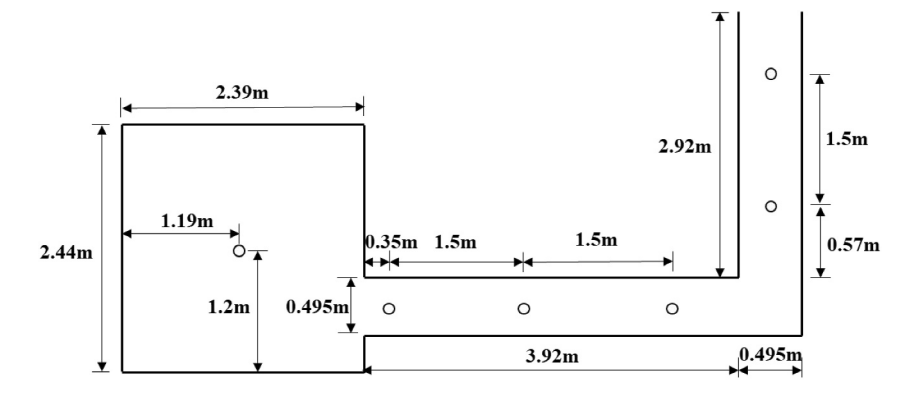


Figure 11. Experimental schematic of L-shaped channel bend dam-break flow.

ZHANG ET AL. 12 of 25

19447973, 2025, 11, Downloaded from https://agupubs.

wiley.com/doi/10.1029/2025WR041568 by Manchester Metropolitan University, Wiley Online Library on [14/11/2025]. See the Terms and Conditions

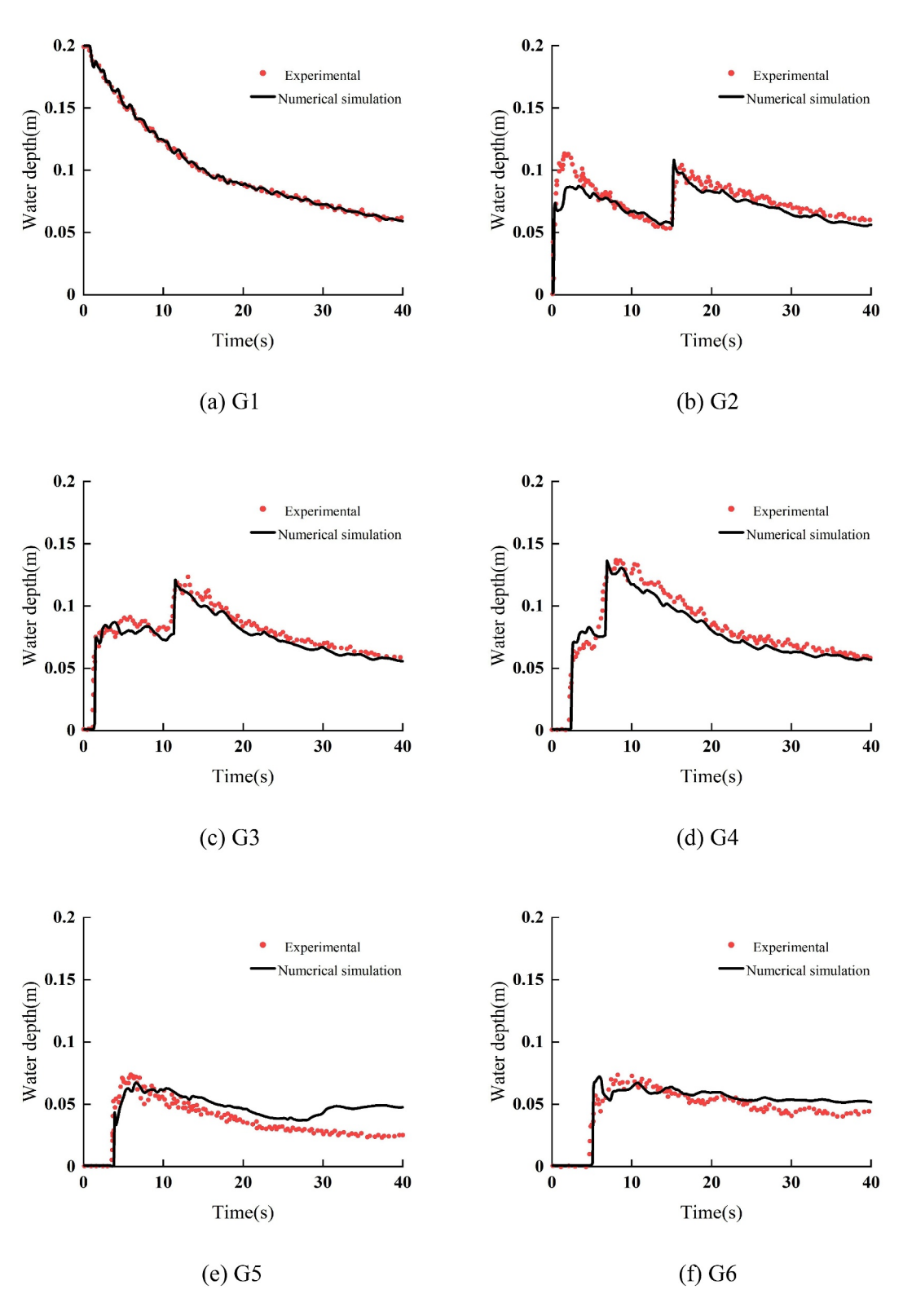
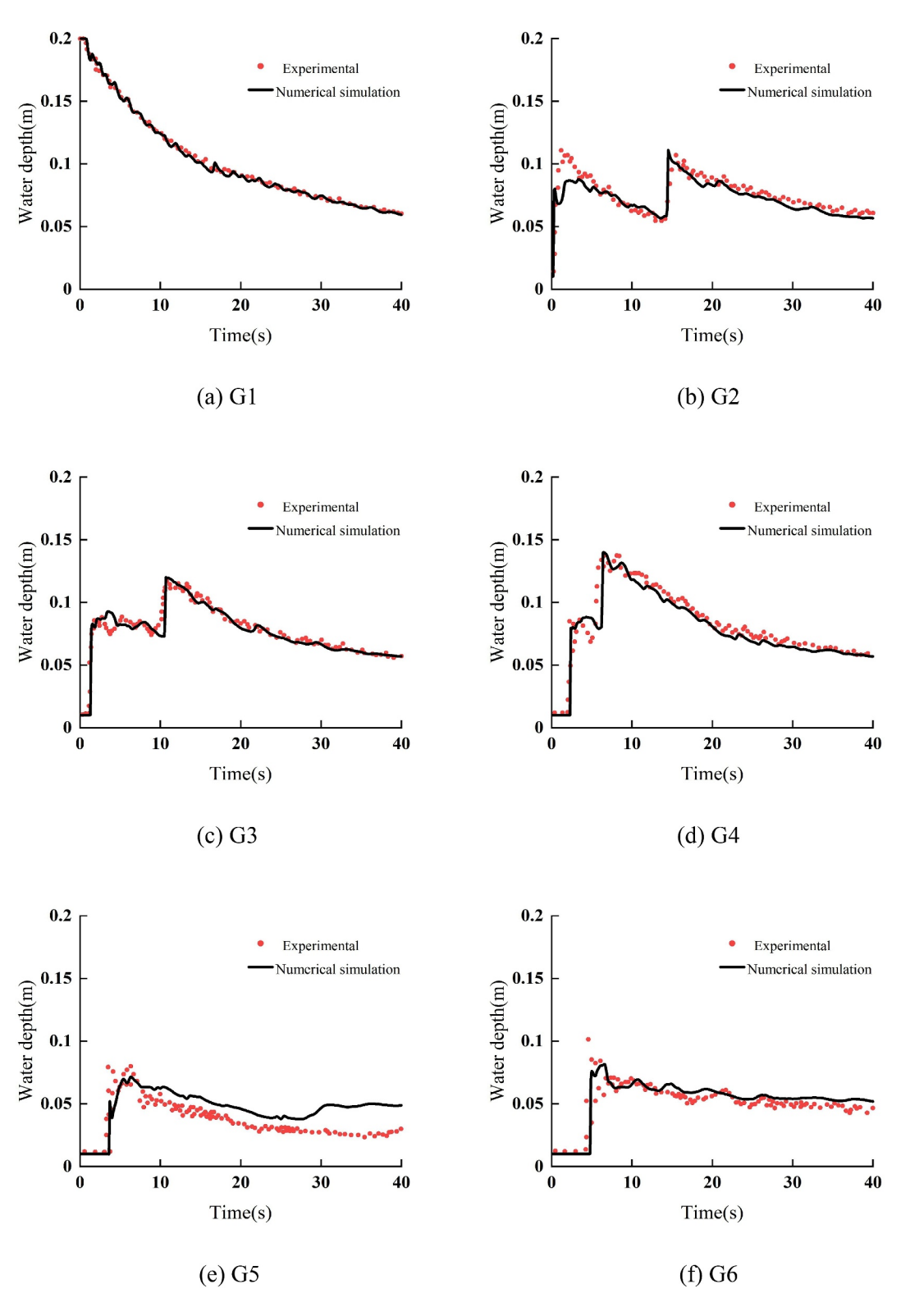


Figure 12. Time histories of water depth from dry-bed test predictions and experimental measurements: (a) G1; (b) G2; (c) G3; (d) G4; (e) G5; and (f) G6.

ZHANG ET AL. 13 of 25

19447973, 2025, 11, Downloaded from https://agupubs.onlinelibrary

wiley.com/doi/10.1029/2025WR041568 by Manchester Metropolitan University, Wiley Online Library on [14/11/2025]. See the Terms and Conditions (https://www.doi.org/10.1029/2025WR041568 by Manchester Metropolitan University, Wiley Online Library on [14/11/2025]. See the Terms and Conditions (https://www.doi.org/10.1029/2025WR041568 by Manchester Metropolitan University, Wiley Online Library on [14/11/2025]. See the Terms and Conditions (https://www.doi.org/10.1029/2025WR041568 by Manchester Metropolitan University, Wiley Online Library on [14/11/2025]. See the Terms and Conditions (https://www.doi.org/10.1029/2025WR041568 by Manchester Metropolitan University, Wiley Online Library on [14/11/2025]. See the Terms and Conditions (https://www.doi.org/10.1029/2025WR041568 by Manchester Metropolitan University, Wiley Online Library on [14/11/2025].



**Figure 13.** Time histories of water depth from wet-bed test predictions and experimental measurements: (a) G1; (b) G2; (c) G3; (d) G4; (e) G5; and (f) G6.

ZHANG ET AL. 14 of 25

19447973, 2025, 11, Downle

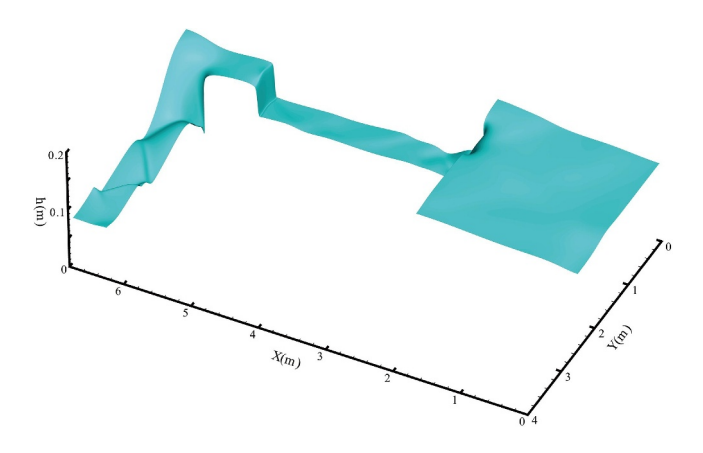


**Figure 14.** 3D water surface plot at t = 7s for wet-bed dam-break flow.

after gate opening, followed by a slower, more gradual decline from 15 to 40s. This behavior indicates that the numerical model precisely reproduces the reservoir's emptying process in a physically plausible way. Furthermore, the water depth at (b) G2, (c) G3, and (d) G4—positions located between the gate and the channel bend-exhibit two distinct rising phases. The first rise is primarily induced by the rapid discharge of water immediately following the dam-break. The second rise appears to result from the complex interaction between the advancing flood wave and the reflected wave generated by the hydraulic resistance at the bend. In contrast, the water depth at (e) G5 and (f) G6—both located downstream of the channel bend—demonstrate a rapid increase in water depth during the initial flooding phase, followed by a gradual recession over time. At G2 and G5, the results show slight differences relative to the experimental measurements. This discrepancy results from the idealized assumption of instantaneous gate removal in the numerical model, whereas the gate opening in the physical experiment involves a finite duration. Additionally, the discrepancies at G2 and G5 between the predicted and

observed water depths likely arise from several factors. These include the neglect of localized head losses at the channel entrance and the 90° bend, the presence of intense turbulence in these regions, and possible air entrainment effects.

Similarly, Figure 13 shows the comparison between the calculated water depth at different measuring points and the experimental data under wet-bed downstream condition. The variation process at G1 is roughly the same as that in the dry-bed condition. A comparison between the simulated and observed primary step changes in water depth at G2-G4, which correspond to the arrival of the bore and its subsequent reflection from the channel elbow, indicates that the wave propagation speeds are accurately captured by the numerical model. Likewise, the water depth at G5 shows a slight overestimation after 10s, a discrepancy that was also reported by Liang and Marche (2009). Overall, there is good consistency between the simulation and the experimental data. Previously discussed factors account for the localized discrepancies. At t = 7s after the dam-break in wet-bed channels, the water surface is displayed in a 3D plot in Figure 14, which illustrates complex flow phenomena.

#### 6.5. 2D Dam-Break Flow Through a Contracting Channel

This case study is based on a physical experiment conducted by A. Bento in Portugal, which investigates dambreak flows in a flat-bed channel with a contraction section. The same computational setup has been adopted in previous studies by Brufau & Garcia-Navarro. (2003) and Rahou and Korichi. (2023). As the dam-break wave propagates, the contraction walls cause partial reflection, resulting in complex flow patterns characterized by both subcritical and supercritical regimes. Figure 15 shows the geometry of the physical model. The total channel length is 19.3 m with a constant width of 0.5 m. At a distance of 6.1 m from the upstream inlet, the dam is situated. A contraction section begins 7.7 m downstream of the dam. It is 1 m long, narrows to 0.1 m in width, and has sidewalls inclined at 45°. The simulation starts with a stationary water surface. The upstream region starts with a water depth of 0.3 m, whereas the downstream bed is initially dry. The channel bed flat, the Manning roughness is set to 0.01. The downstream outlet is defined as a free outflow, whereas solid wall boundaries are applied elsewhere. To capture water depth variations, four gauging points (S1, S2, S3, and S4)

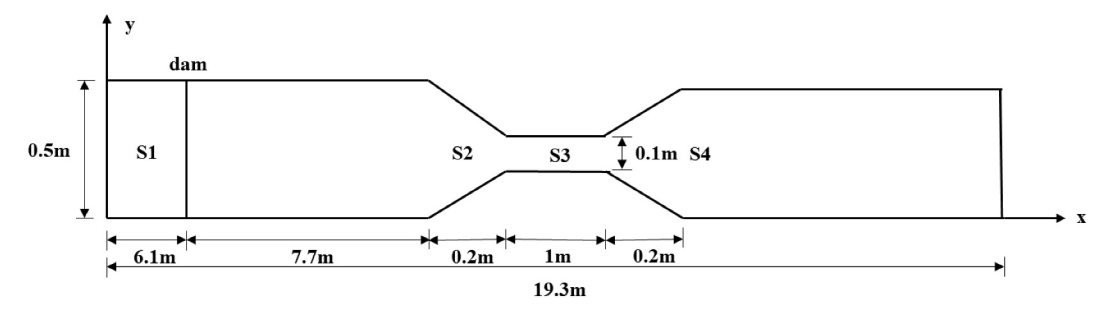


Figure 15. Physical model and measurement points.

ZHANG ET AL. 15 of 25

19447973, 2025, 11, Downlo

itan University, Wiley Online Library on [14/11/2025]. See the Terms

Table 3 Gauging Po	oint Locations			
Points	S1	S2	S3	S4
x	5.1	12.2	14.7	16.6
у	0.25	0.25	0.25	0.25

are placed along the centerline of the channel. Refer to Table 3 for their specific positions: S1 is located upstream reservoir, S2 at the entrance of the contraction, S3 at the midpoint of the contraction, and S4 downstream of the contraction section.

In simulations, a uniform grid of  $386 \times 10$  cells is used to discretize the channel, with a time step of 0.0001s. The reference length  $h_0$  is 0.3 m, and the relaxation parameter  $\tau = 0.00025$ . The dry threshold depth  $h_{\rm dry}$  is set to

0.001 m, and the wet threshold depth  $h_{\rm wet}$  is set to 0.004 m. Following the instantaneous dam breach, the simulation runs for 10s.

Figure 16 presents a comparison of simulated water depth variations with experimental data at four measurement points. At S1, the water level changes relatively smoothly. At S2, the wave produced by the dam breach begins to show its effects around 3s, followed by a sudden rise in water depth at t = 8s due to a reflected wave caused by the channel contraction, which subsequently propagate upstream. At S3, a noticeable surge in water depth takes place after 4.2s. At S4, a slight diffracted shock wave appears, followed by a gradual stabilization of the water

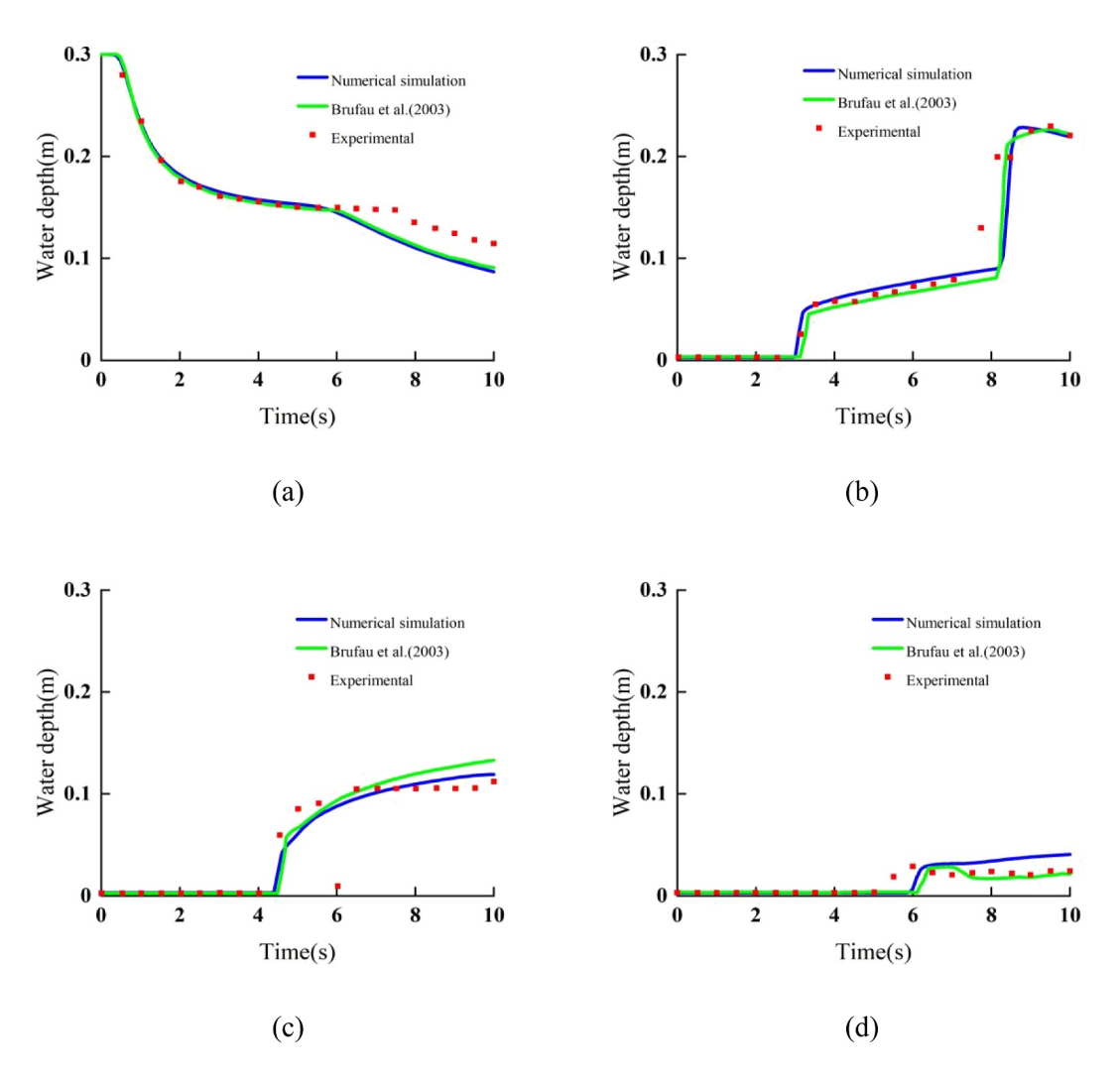


**Figure 16.** Comparison of experimental and simulated water depths at gauging points S1(a), S2(b), S3(c), and S4(d) over a 10s period.

ZHANG ET AL. 16 of 25

19447973, 2025, 11, Downloaded from https://agupubs

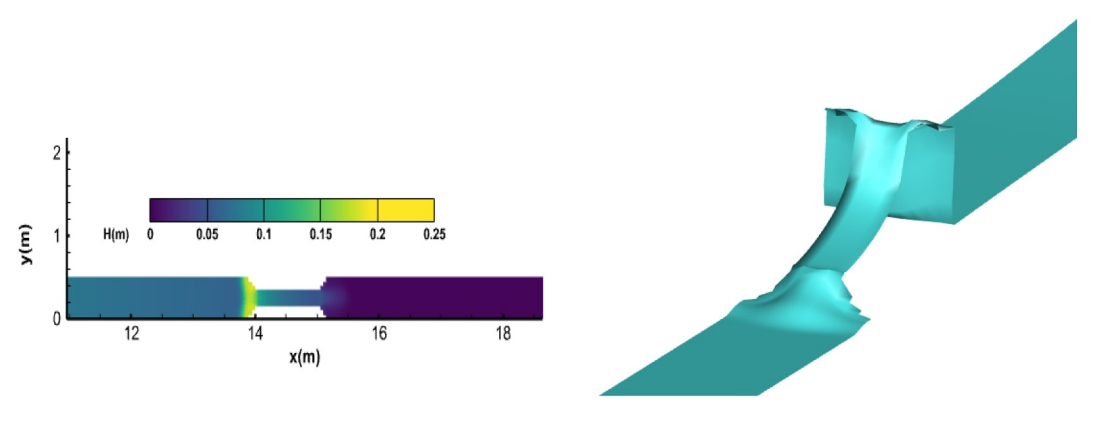


**Figure 17.** Water depth and free surface at t = 5s.

surface. Overall, the predicted water depths demonstrate close consistency with the experimental data and align with the simulation results by Brufau and Garcia-Navarro (2003). Figures 17 and 18 show the free surface and water depth at t=5s and t=10s, respectively. The model is shown to effectively capture the processes involved in wetting and drying, as reflected by these results. To enable a quantitative evaluation, the relative error  $E_r$  is employed to assess the performance of the methods. Table 4 shows that, at most locations, the predictions of the DBM exhibit smaller errors with respect to the experimental data compared to the results reported by Brufau & Garcia-Navarro. (2003). In addition, the Froude numbers at the four points in Figure 19 also reflect different flow dynamic characteristics during the 10s period.

## 6.6. Two-Dimensional Flooding Around Three Mounds

The last case is a two-dimensional flooding over dry terrain with three mounds. Due to the complexity of the flow, this problem lacks an explicit analytical solution. However, numerical results reported by Brufau and Garcia-Navarro (2003), Delis and Katsaounis (2005), Gallardo et al. (2007), and Liang and Borthwick (2009) provide a basis for qualitative comparison with our numerical simulations.

The channel is 30 m wide and 75 m long, and the topography with three mounds is described by  $zb(x, y) = \max(0, m_1, m_2, m_3)$ , where

$$m_1 = 1 - 0.125\sqrt{(x - 30)^2 + (y - 6)^2},$$
 (16)

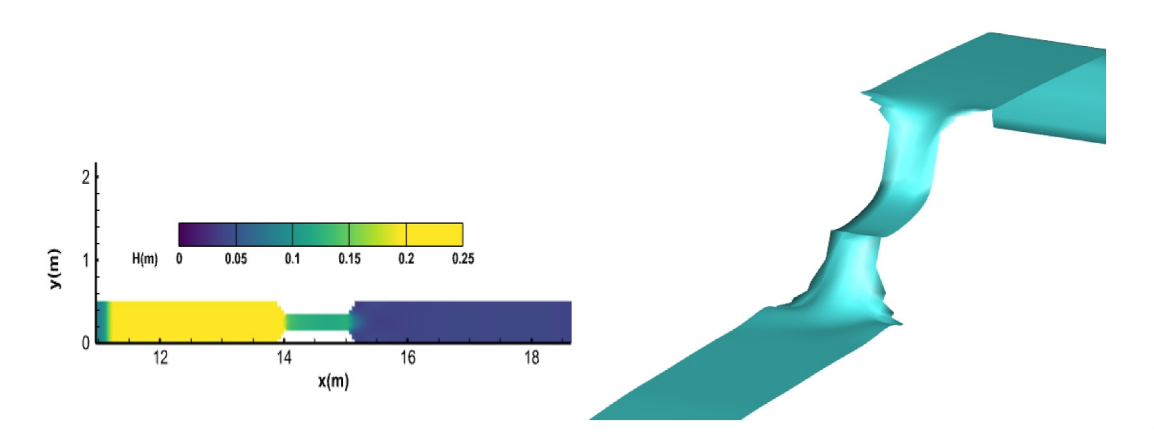


**Figure 18.** Water depth and free surface at t = 10s.

ZHANG ET AL. 17 of 25

19447973, 2025, 11, Downle

<b>Table 4</b> <i>The Relative Er</i>	$ror E_r$ for Two Methods	
	DBM	Brufau et al.
S1	0.02756	0.03106
S2	0.03618	0.06774
S3	0.41788	0.77022
S4	0.11077	0.08648

$$m_2 = 1 - 0.125\sqrt{(x - 30)^2 + (y - 24)^2},$$
 (17)

and,

$$m_3 = 3 - 0.3\sqrt{(x - 47.5)^2 + (y - 15)^2}$$
 (18)

Initially, a dam is placed at x = 16 m, retaining still water with a surface elevation of 1.875 m. The channel bottom surface and the upstream water held

stationary by the dam are shown in Figure 20. At t = 0s, the dam undergoes instantaneous failure, initiating the flood wave. The Manning coefficient  $n_b = 0.018$  is adopted to represent the roughness of the bed.

A uniform mesh of  $750 \times 300$  cells is used to discretize the full domain and the time step is 0.0001s. The simulation runs for a total duration of 300s. Transmissive boundary condition is applied at the downstream boundary. The dry and wet threshold water depths are set to  $h_{\rm dry} = 0.001$  m and  $h_{\rm wet} = 0.02$  m, respectively. The reference length is  $h_0 = 1$  m, and  $\tau = 0.0004$ .

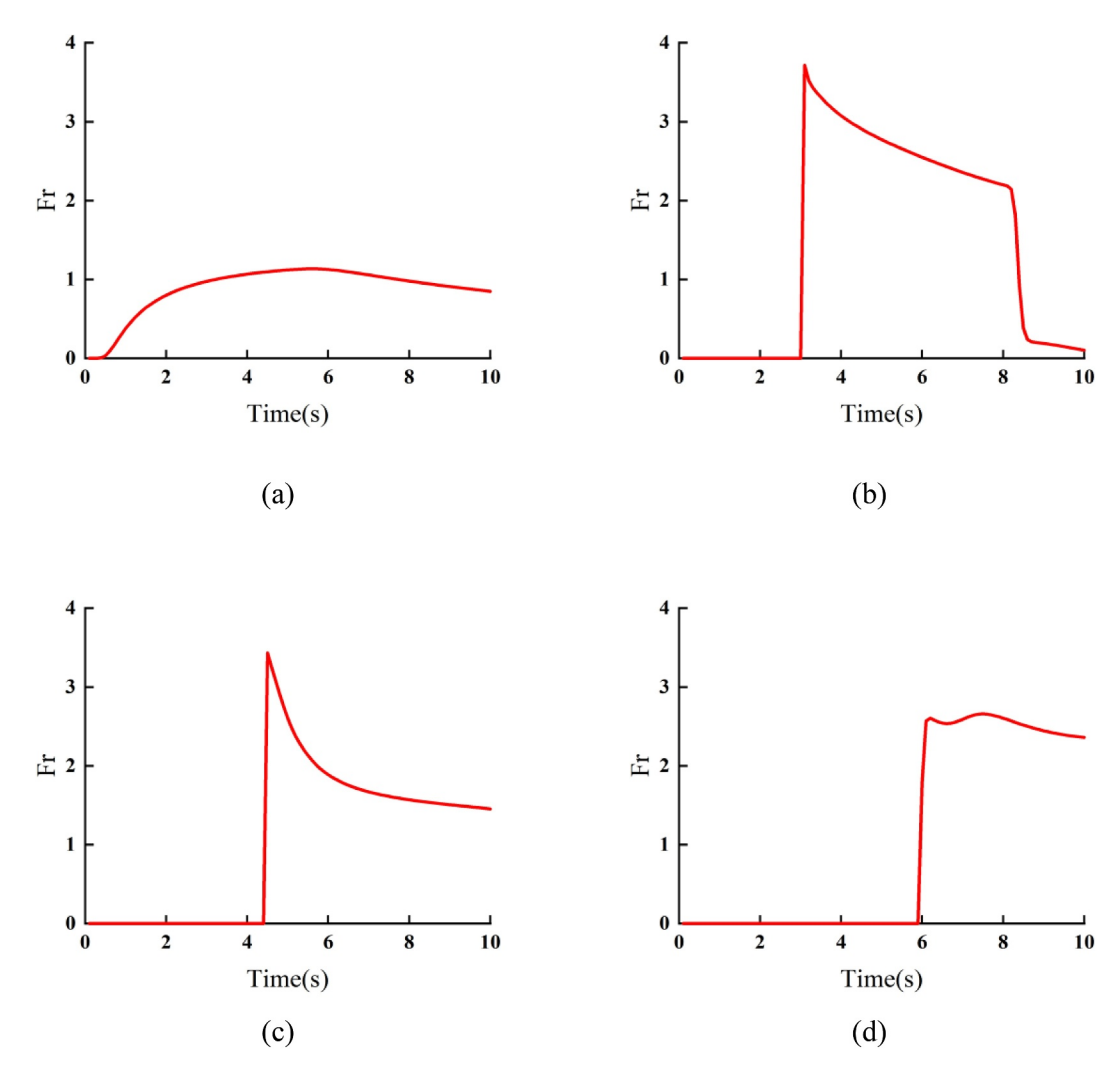


Figure 19. Predicted Froude numbers at measuring points S1(a), S2(b), S3(c), S4(d) within 10s.

ZHANG ET AL. 18 of 25

19447973, 2025, 11, Downloaded from https://agupubs.

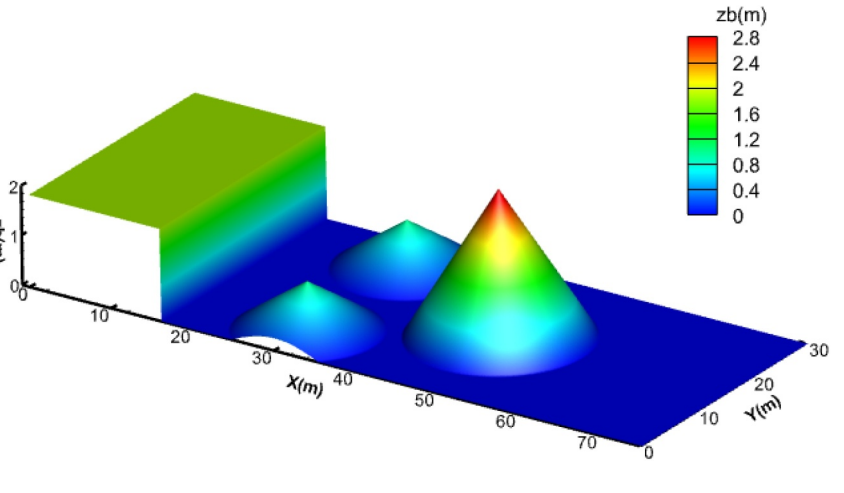


Figure 20. Initial state of complex terrain.

Figure 21 shows the wetting and drying transitions and evolution of wave propagation until reaching a steady state. The simulation results show good qualitative agreement with those reported by Delis and Katsaounis (2005) and Liang and Borthwick (2009). Immediately after the dam breach, the floodplain is inundated by a flood wave with a leading wet-dry front. By t = 2s, the toe of two small mounds is reached by the flow front, which then starts to rise over them. A shock wave reflecting upstream is produced due to the interplay between the flow and the terrain, generating a small hydraulic jump in the front of the two small mounds. Meanwhile, the wet-dry front partially progresses downstream, passing between the mounds. By t = 6s, the small mounds are fully inundated, and the advancing wet-dry front reaches the base of the large mound. Propelled by the flood wave's momentum, the leading edge climbs over halfway up the large mound, as water flows around both flanks. Curved reflected bores continue moving upstream, interacting with each other and with the container walls. At t = 12s, the water passing on both sides of the large mound begins to enter the downstream area behind it. An almost straight bore traveling upstream is formed by the merging of waves reflected from the small mounds, while the main flood wave reflects and generates another bore traveling back toward the source. The highest water level near the mound decreases as this new bore moves upstream. Subsequent wave interactions with other waves, boundaries, and terrain, along with bed friction, resulting in energy dissipation and gradual stabilization of the flow. By t = 300s, the flow stabilizes, and the tops of the small mounds become exposed again. The numerical model successfully captures the intricate wetting and drying behavior throughout the simulation, and its capability to preserve mass is further examined. As in Delis and Katsaounis (2005), the mass error is quantified using the initial mass volume  $(V_{in})$  and the volume at each time step  $(V_{nu})$ , and its temporal evolution is presented. The error is computed as Mass error(%) =  $\frac{V_{nu} - V_{in}}{V_{in}}$ . Based on this definition, the time history of the error is plotted to assess the conservation property of the scheme. It is further illustrated in Figure 22 that the proposed scheme exhibits strong mass conservation, with only minor errors observed even during the progression over the initially dry region.

# 7. Synthesis and Discussion

The comprehensive suite of six benchmark cases presented in Section 6 collectively demonstrates the reliability, accuracy, and versatility of the proposed discrete Boltzmann model (DBM) for shallow water flows involving wetting and drying interfaces. Each case was carefully selected to test a distinct aspect of the model's performance under various flow regimes and boundary conditions. A summary of all validation cases, including their key purposes and findings, is provided in Table 5 to facilitate cross-comparison and highlight the distinct role of each example.

ZHANG ET AL. 19 of 25

19447973, 2025, 11, Downolated from http://sgupubs.on/inibitary.wiely.com/doi/10.109.2025WR041568 by Manchester Metopolian University, Wiley Online Library on [4/11/2025]. See the Terms and Conditions (https://onlinelibrary.wiely.com/emms-ad-conditions) on Wiley Online Library for rules of use; OA articles are governed by the applicable Creative Commons License

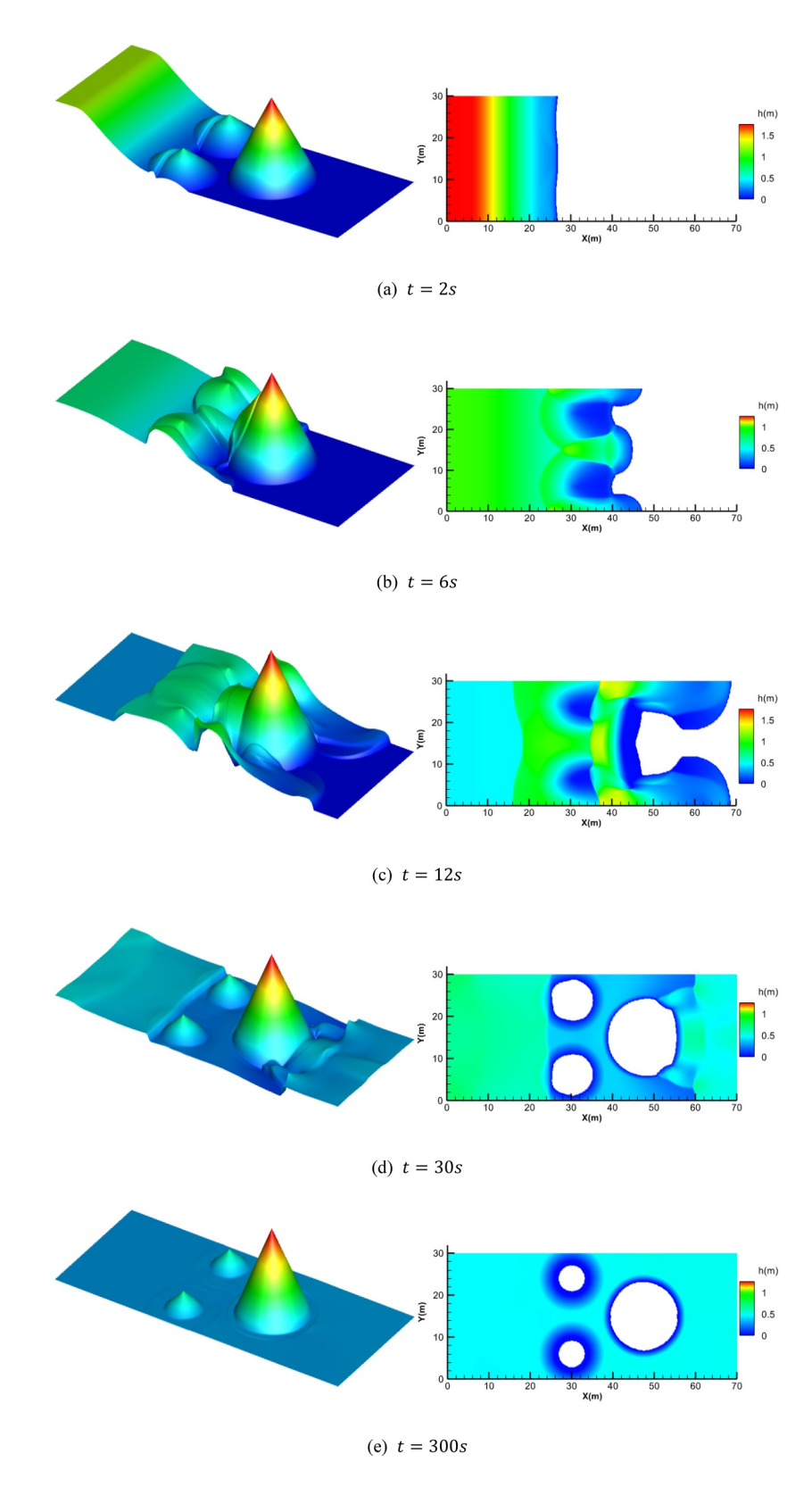


Figure 21. Three-hump flooding propagation: 3D view of water surface elevation and plan views of water depth at selected time instants.

ZHANG ET AL. 20 of 25

19447973, 2025, 11, Downloaded from https://agupubs

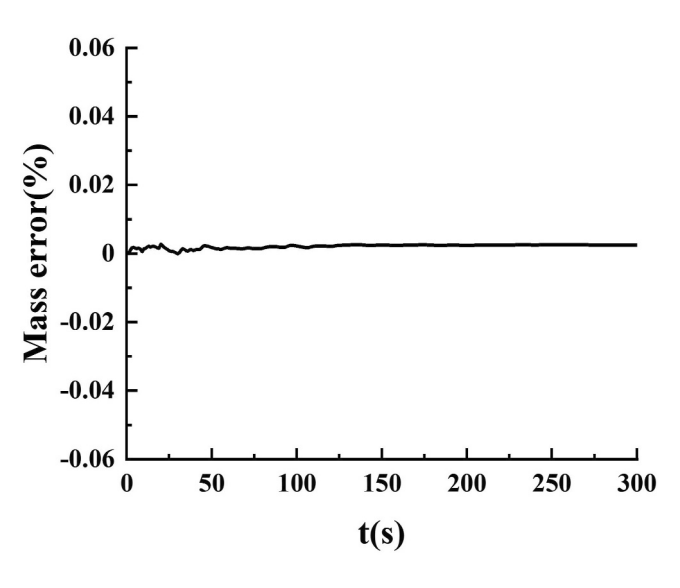


Figure 22. Time history of mass error during the simulation.

The 1D tests (Cases 6.1–6.3) confirm the model's capacity to handle flows over non-uniform beds with strong wet–dry transitions, slope effects, and frictional influences, ensuring numerical stability and close agreement with laboratory data. The 2D cases (6.4–6.6) extend the validation to complex geometries, including channel bends, contractions, and irregular topography. The results consistently show that the model accurately captures wave propagation, flow separation, and inundation processes under both wet and dry initial conditions.

Collectively, these examples verify key numerical features such as stability across a wide range of slopes, and the robustness of the wetting–drying scheme. The consistency of results across all cases highlights the method's general applicability to realistic hydrodynamic problems. Therefore, Table 5 and the above analyses together provide comprehensive synthesis demonstrating that, although multiple examples are presented, each serves a unique role in validating the proposed approach across diverse flow conditions.

#### 8. Conclusions

This study presents a detailed integration of an effective wetting and drying tracking strategy into a discrete Boltzmann model (DBM) for shallow water flows, aimed at accurately simulating wet–dry transitions. The performance of the proposed approach is evaluated through six classical benchmark test cases. Numerical results demonstrate that the DBM, when coupled with an appropriate wetting and drying scheme, successfully capture both subcritical and supercritical flows over initially dry and complex topographies. Among the parameters governing the wetting-drying scheme, the wet threshold water depth  $h_{\text{wet}}$  plays a crucial role in determining simulation accuracy, and it is required that  $h_{\text{wet}}$  be greater than the dry threshold water depth  $h_{\text{dry}}$ . In general, a smaller value of  $h_{\text{wet}}$  tends to yield more accurate predictions. However, excessively small  $h_{\text{wet}}$  values may lead to unrealistic high flow velocities and unstable flow regimes, ultimately causing numerical instability. Therefore, properly selecting the two threshold water depths is vital for balancing computational stability with accurate simulation results. Within this context, the DBM model demonstrates robust performance in dealing with wet–dry transitions over complex terrain, highlighting its potential as an effective alternative to conventional finite volume and finite element methods for shallow-water flow simulations.

ZHANG ET AL. 21 of 25

Summar	ry of Validation C	Summary of Validation Cases and Their Key Findings		
Case	Dimension	Topography type	Validation focus	Key findings
6.1	ID	Flat bed with triangular obstacle	Basic validation, influence of obstacles and friction, experimental comparison showing the sensitivity of wetdry parameters	Achieved excellent agreement with experiments and identified optimal wet-dry thresholds for stability.
6.2	1D	Varying sloped bed	Verification of non-steady boundary and slope variation	Excellent agreement with previous studies; correctly captures tidal run-up and retreat.
6.3	1D	Non-uniform terrain with elevation steps	Test performance in dynamic wetting-drying with irregular topography	Demonstrates strong predictive capability for transient wet-dry transitions and Froude number variation.
6.4	2D	L-shaped channel	Validate flow around sharp bends and reflection effects	Reproduced complex flow interactions and wave reflections with high fidelity.
6.5	2D	Contracting channel	Test performance under mixed flow regimes	Accurately resolved shock reflections and subcritical-supercritical transitions with smaller errors than previous models.
9.9	2D	Complex terrain with three mounds	Demonstrate capability in large-scale inundation	Captured multi-wave interactions and ensured strong mass conservation.

22 of 25

19447973, 2025, 11, Downloaded from https://agupub

#### **Conflict of Interest**

The authors declare no conflicts of interest relevant to this study.

# **Data Availability Statement**

The used DBM codes in this paper are available online at https://doi.org/10.5281/zenodo.17211664 (The open-source software program) and were collected by the author (Zhang, 2025).

#### Acknowledgments

Present research is partially supported by Inner Mongolia Department of Science and Technology 2024 major projects to prevent and control sand demonstration "unveiled marshal" project (No:2024JBGS0016), National Foreign Expert Program (No: H20240398) and Xianyang Science and Technology Bureau (No: L2024-ZDYF-ZDYF-SF-0042).

## References

- Aizinger, V., & Dawson, C. (2002). A discontinuous Galerkin method for two-dimensional flow and transport in shallow water. Advances in Water Resources, 25(1), 67–84. https://doi.org/10.1016/s0309-1708(01)00019-7
- Aureli, F., Mignosa, P., & Tomirotti, M. (1999). Dam-break flows in presence of abrupt bottom variations. In *Proceedings of XXVIII IAHR cong* 1999 (pp. 163–171).
- Brufau, P., & Garcia-Navarro, P. (2003). Unsteady free surface flow simulation over complex topography with a multidimensional upwind technique. *Journal of Computational Physics*, 186(2), 503–526.
- Brufau, P., Vazquez-Cendon, M. E., & Garcia-Navarro, P. (2002). A numerical method for the flooding and drying of irregular domains. International Journal for Numerical Methods in Fluids. 39(3), 247–275.
- Bulatov, O. V., & Elizarova, T. G. (2011). Regularized shallow water equations and an efficient method for numerical simulation of shallow water flows. Computational Mathematics and Mathematical Physics, 51(1), 160–173. https://doi.org/10.1134/s0965542511010052
- Castro, M. J., Ferreiro, A. M. F., García-Rodríguez, J. A., González-Vida, J. M., Macías, J., Parés, C., & Vázquez-Cendón, M. E. (2005). The numerical treatment of wet/dry fronts in shallow flows: Application to one-layer and two-layer systems. *Mathematical and Computer Modelline*, 42(3–4), 419–439.
- Cozzolino, L., Morte, R. D., Del, G. G., Palumbo, A., & Pianese, D. (2012). A well-balanced spectral volume scheme with the wetting–drying property for the shallow-water equations. *Journal of Hydroinformatics*, 14(3), 745–760.
- Delis, A. I., & Katsaounis, T. (2005). Numerical solution of the two-dimensional shallow water equations by the application of relaxation methods. *Applied Mathematical Modelling*, 29(8), 754–783. https://doi.org/10.1016/j.apm.2004.11.001
- Dellar, P. J. (2002). Nonhydrodynamic modes and a priori construction of shallow water lattice Boltzmann equations. *Physics Reviews E.*, 65(3), 036309. https://doi.org/10.1103/physreve.65.036309
- Frazao, S. S., & Zech, Y. (2002). Dam break in channels with 90 bend. *Journal of Hydraulic Engineering*, 128(11), 956–968. https://doi.org/10.1061/(asce)0733-9429(2002)128:11(956)
- Funke, S. W., Pain, C. C., Kramer, S. C., & Piggott, M. D. (2011). A wetting and drying algorithm with a combined pressure/free-surface formulation for non-hydrostatic models. *Advances in Water Resources*, 34(11), 1483–1495. https://doi.org/10.1016/j.advwatres.2011.08.007
- Gallardo, J. M., Pares, C., & Castro, M. (2007). On a well-balanced high-order finite volume scheme for shallow water equations with topography and dry areas. *Journal of Computational Physics*, 227(1), 574–601. https://doi.org/10.1016/j.jcp.2007.08.007
- Gottardi, G., & Venutelli, M. (2004). Central scheme for two-dimensional dam-break flow simulation. Advances in Water Resources, 27(3), 259–268. https://doi.org/10.1016/j.advwatres.2003.12.006
- Guo, Z. L., Zheng, C. G., & Shi, B. C. (2002). Non-equilibrium extrapolation method for velocity and pressure boundary conditions in the lattice Boltzmann method. *Chinese Physics*, 11(4), 366–374. https://doi.org/10.1088/1009-1963/11/4/310
- He, J., & Xin, W. J. (2009). Treatment of wet-dry boundaries in shallow water equations. In *Proceedings of the 9th national conference on hydrodynamics & 22nd national symposium on hydrodynamics*. China.
- Hedjripour, A. H., (2018). Lattice boltzmann modelling of supercritical shallow water flows.
- Hedjripour, A. H., Callaghan, D. P., & Baldock, T. E. (2016). Generalized transformation of the lattice Boltzmann method for shallow water flows. *Journal of Hydraulic Research*, 54(4), 371–388. https://doi.org/10.1080/00221686.2016.1168881
- Heniche, M., Secretan, Y., Boudreau, P., & Leclerc, M. (2000). A two-dimensional finite element drying-wetting shallow water model for rivers and estuaries. *Advances in Water Resources*, 23(4), 359–372. https://doi.org/10.1016/s0309-1708(99)00031-7
- Hiver, J. M. (2000). Adverse-slope and slope (bump). In S. Soares-Frazao, M. Morris, & Y. Zech (Eds.), Concerted action on dam break modelling: Objectives [CD-ROM].
- Hou, J., Simons, F., Mahgoub, M., & Hinkelmann, R. (2013). A robust well-balanced model on unstructured grids for shallow water flows with wetting and drying over complex topography. Computer Methods in Applied Mechanics and Engineering, 257, 126–149. https://doi.org/10.1016/j.cma.2013.01.015
- Jiang, X., Chen, P., Cheng, H., Chen, X., Chen, H., Zhu, Z., & Zou, Z. (2023). Dry and wet boundary treatment and improvement of a TVD-MacCormack scheme in shallow water flow. *International Journal for Numerical Methods in Fluids*, 95(6), 917–936. https://doi.org/10.1002/fld.5174
- Kalita, H. M., & Sarma, A. K. (2018). An implicit scheme for shallow water flow with wet dry interface. Water Resources, 45(1), 61–68. https://doi.org/10.1134/s0097807818010104
- Kefayati, G., Tolooiyan, A., & Dyson, A. P. (2023). Finite difference lattice Boltzmann method for modeling dam break debris flows. *Physics of Fluids*, 35(1), 013102. https://doi.org/10.1063/5.0130947
- Kesserwani, G., & Wang, Y. (2014). Discontinuous Galerkin flood model formulation: Luxury or necessity? Water Resources Research, 50(8), 6522–6541. https://doi.org/10.1002/2013wr014906
- La Rocca, M., Montessori, A., Prestininzi, P., & Succi, S. (2015). A multispeed Discrete Boltzmann model for transcritical 2D shallow water flows. *Journal of Computational Physics*, 284, 117–132. https://doi.org/10.1016/j.jcp.2014.12.029
- Le, H. A., Lambrechts, J., Ortleb, S., Gratiot, N., Deleersnijder, E., & Soares-Frazão, S. (2020). An implicit wetting-drying algorithm for the discontinuous Galerkin method: Application to the Tonle Sap, Mekong River Basin. Environmental Fluid Mechanics, 20(4), 923–951. https://doi.org/10.1007/s10652-019-09732-7
- Leclerc, M., Bellemare, J. F., Dumas, G., & Dhatt, G. (1990). A finite element model of estuarian and river flows with moving boundaries. Advances in Water Resources, 13(4), 158–168. https://doi.org/10.1016/0309-1708(90)90039-7
- Li, S., Huang, P., & Li, J. (2015). A modified lattice Boltzmann model for shallow water flows over complex topography. *International Journal for Numerical Methods in Fluids*, 77(8), 441–458. https://doi.org/10.1002/fld.3991

ZHANG ET AL. 23 of 25

- Liang, Q., & Borthwick, A. G. L. (2009). Adaptive quadtree simulation of shallow flows with wet-dry fronts over complex topography. Computers & Fluids, 38(2), 221–234. https://doi.org/10.1016/j.compfluid.2008.02.008
- Liang, Q., & Marche, F. (2009). Numerical resolution of well-balanced shallow water equations with complex source terms. Advances in Water Resources, 32(6), 873–884. https://doi.org/10.1016/j.advwatres.2009.02.010
- Liang, S. J., Young, C. C., Dai, C., Wu, N. J., & Hsu, T. W. (2020). Simulation of ocean circulation of Dongsha water using non-hydrostatic shallow-water model. Water, 12(10), 2832. https://doi.org/10.3390/w12102832
- Liao, C. B., Wu, M. S., & Liang, S. J. (2007). Numerical simulation of a dam break for an actual river terrain environment. Hydrological Processes, 21(4), 447–460. https://doi.org/10.1002/hyp.6242
- Liu, H., Zhang, J., & Shafiai, S. H. (2016). A second-order treatment to the wet–dry interface of shallow water. *Journal of Hydrology*, 536, 514–523. https://doi.org/10.1016/j.jhydrol.2016.03.014
- Liu, H., Zhang, J., Wang, H., Ding, Y., & Yi, Y. (2017). Numerical modeling of the tidal wave run-up and the eelgrass habitat at the Laizhou Bay. Ecological Modelling, 360, 378–386. https://doi.org/10.1016/j.ecolmodel.2017.02.025
- Liu, H., & Zhou, J. G. (2010). Burrows R. Lattice Boltzmann simulations of the transient shallow water flows. *Advances in Water Resources*, 33(4), 387–396. https://doi.org/10.1016/j.advwatres.2010.01.005
- Liu, H., & Zhou, J. G. (2014). Lattice Boltzmann approach to simulating a wetting-drying front in shallow flows. *Journal of Fluid Mechanics*, 743, 32–59. https://doi.org/10.1017/jfm.2013.682
- Liu, X. (2020). A well-balanced and positivity-preserving numerical model for shallow water flows in channels with wet–dry fronts. *Journal of Scientific Computing*, 85(3), 60. https://doi.org/10.1007/s10915-020-01362-2
- Liu, Y., Chai, Z., Guo, X., & Shi, B. (2021). A lattice Boltzmann model for the viscous shallow water equations with source terms. *Journal of Hydrology*, 598, 126428. https://doi.org/10.1016/j.jhydrol.2021.126428
- Liu, Y., Zhou, J., Song, L., Zou, Q., Liao, L., & Wang, Y. (2013). Numerical modelling of free-surface shallow flows over irregular topography with complex geometry. *Applied Mathematical Modelling*, 37(23), 9482–9498. https://doi.org/10.1016/j.apm.2013.05.001
- Magdalena, I., & Pebriansyah, M. F. E. (2022). Numerical treatment of finite difference method for solving dam break model on a wet-dry bed with an obstacle. Results in Engineering, 14, 100382.
- Mcnamara, G. R., & Zanetti, G. (1998). Use of the Boltzmann equation to simulate lattice gas automata. *Physical Review Letters*, 61(20), 2332–2335, https://doi.org/10.1103/physreylett.61.2332
- Meng, J., Gu, X. J., Emerson, D. R., Peng, Y., & Zhang, J. (2018). Discrete Boltzmann model of shallow water equations with polynomial equilibria. *International Journal of Modern Physics C*, 29(9), 1850080. https://doi.org/10.1142/s0129183118500808
- Oey, L. Y. (2005). A wetting and drying scheme for POM. Ocean Modelling, 9(2), 133-150. https://doi.org/10.1016/j.ocemod.2004.06.002
- Peng, Y., Ouyang, J. Y., Guan, M. F., Wang, B., & Rubinato, M. (2024). Experimental and numerical estimation of velocity and concentration distributions in partially vegetated open channels. *Journal of Hydrology*, 628, 130537. https://doi.org/10.1016/j.jhydrol.2023.130537
- Peng, Y., Zhou, J. G., Zhang, J. M., & Liu, H. (2014). Lattice Boltzmann modeling of shallow water flows over discontinuous beds. *International Journal for Numerical Methods in Fluids*, 75(8), 608–619. https://doi.org/10.1002/fld.3911
- Perumal, D. A., & Dass, A. K. (2015). A review on the development of lattice Boltzmann computation of macro fluid flows and heat transfer. Alexandria Engineering Journal, 54(4), 955–971.
- Qian, Y. H., Dhumieres, D., & Lallemand, P. (1992). Lattice BGK models for navier-stokes equation. Europhysics Letters, 17(6), 479–484. https://doi.org/10.1209/0295-5075/17/6/001
- Quecedo, M., & Pastor, M. (2002). A reappraisal of Taylor–Galerkin algorithm for drying–wetting areas in shallow water computations. International Journal for Numerical Methods in Fluids, 38(6), 515–531. https://doi.org/10.1002/fld.225
- Rahou, I., & Korichi, K. (2023). Comparative analysis of numerical solutions of 2D unsteady dambreak waves using FVM and SPH method. Journal of Hydrology and Hydromechanics, 71(3), 305–315. https://doi.org/10.2478/johh-2023-0005
- Rebollo, T. C., Nieto, E. D. F., & Mármol, M. G. (2003). A flux-splitting solver for shallow water equations with source terms. *International Journal for Numerical Methods in Fluids*. 42(1), 23–55.
- Rocca, M. L., Adduce, C., Lombardi, V., Sciortino, G., & Hinkelmann, R. (2012). Development of a lattice Boltzmann method for two-layered shallow-water flow. *International Journal for Numerical Methods in Fluids*, 70(8), 1048–1072. https://doi.org/10.1002/fld.2742
- Ru, Z., Liu, H., Yang, W., & Leng, F. (2024). A novel framework of the lattice Boltzmann model for multilayer shallow water systems. *Physics of Fluids*, 36(9), 097170. https://doi.org/10.1063/5.0227227
- Shafiai, S. H. (2011). Lattice Boltzmann method for simulating shallow free surface flows involving wetting and drying. University of Liverpool. Sleigh, P., Gaskell, P., Berzins, M., & Wright, N. G. (1998). An unstructured finite-volume algorithm for predicting flow in rivers and estuaries. Computers & Fluids, 27(4), 479–508. https://doi.org/10.1016/s0045-7930(97)00071-6
- Sobey, R. J. (2009). Wetting and drying in coastal flows. Coastal Engineering, 56(5–6), 565–576. https://doi.org/10.1016/j.coastaleng.2008.
- Song, L., Zhou, J., Guo, J., Zou, Q., & Liu, Y. (2011). A robust well-balanced finite volume model for shallow water flows with wetting and drying over irregular terrain. Advances in Water Resources, 34(7), 915–932. https://doi.org/10.1016/j.advwatres.2011.04.017
- Stipić, D., Budinski, L., & Fabian, J. (2022). Sediment transport and morphological changes in shallow flows modelled with the lattice Boltzmann method. *Journal of Hydrology*, 606, 127472. https://doi.org/10.1016/j.jhydrol.2022.127472
- Thömmes, G., Seaid, M., & Banda, M. K. (2007). Lattice Boltzmann methods for shallow water flow applications. *International Journal for Numerical Methods in Fluids*, 55(7), 673–692. https://doi.org/10.1002/fld.1489
- Thorimbert, Y., Lätt, J., & Chopard, B. (2019). Coupling of lattice Boltzmann shallow water model with lattice Boltzmann free-surface model. *Journal of Computer Science*, 33, 1–10.
- Vater, S., Beisiegel, N., & Behrens, J. (2015). A limiter-based well-balanced discontinuous Galerkin method for shallow-water flows with wetting and drying: One-dimensional case. Advances in Water Resources, 85, 1–13. https://doi.org/10.1016/j.advwatres.2015.08.008
- Venturi, S., (2018). Lattice Boltzmann shallow water equations for large scale hydraulic analysis.
- Waterways Experiment Station. (1960, 1961). Floods resulting from suddenly breached dams (Miscellaneous Paper N, 2-374, Report 1: Conditions of minimum resistance; Report 2: Conditions of high resistance). US Army Corps of Engineering.
- Wood, A., & Wang, K. H. (2015). Modeling dam-break flows in channels with 90 degree bend using an alternating-direction implicit based curvilinear hydrodynamic solver. Computers & Fluids, 114, 254–264. https://doi.org/10.1016/j.compfluid.2015.03.011
- Xia, J., Falconer, R. A., Lin, B., & Tan, G. (2010). Modelling flood routing on initially dry beds with the refined treatment of wetting and drying. International Journal of River Basin Management, 8(3–4), 225–243. https://doi.org/10.1080/15715124.2010.502121
- Zhang, M., & Wu, W. M. (2011). A two dimensional hydrodynamic and sediment transport model for dam break based on finite volume method with quadtree grid. *Applied Ocean Research*, 33(4), 297–308. https://doi.org/10.1016/j.apor.2011.07.004
- Zhang, T. (2025). DBM codes for shallow water flow simulation (version 1.0.0) [Software]. Zenodo. https://doi.org/10.5281/zenodo.17211664

ZHANG ET AL. 24 of 25

- Zhang, T., Peng, Y., Meng, J., Zhang, K., & Fei, Y. (2025). Wetting-drying scheme for discrete Boltzmann modeling of shallow water flows. *Journal of Hydrology*, 661, 133592. https://doi.org/10.1016/j.jhydrol.2025.133592
- Zhao, D. H., Shen, H. W., Tabios, G. Q., Lai, J. S., & Tan, W. Y. (1994). Finite-volume two-dimensional unsteady flow model for river basins. *Journal of Hydraulic Engineering*, 120(7), 863–883. https://doi.org/10.1061/(asce)0733-9429(1994)120:7(863)
- Zhou, J. G. (2002). A lattice Boltzmann model for the shallow water equations. Computer Methods in Applied Mechanics and Engineering, 191(32), 3527–3539. https://doi.org/10.1016/s0045-7825(02)00291-8
- Zhou, J. G., Causon, D. M., Mingham, C. G., & Ingram, D. (2004). Numerical prediction of dam-break flows in general geometries with complex bed topography. *Journal of Hydraulic Engineering*, 130(4), 332–340. https://doi.org/10.1061/(asce)0733-9429(2004)130:4(332)

ZHANG ET AL. 25 of 25